The Astrophysical Journal, 872:40 (21pp), 2019 February 10 https://doi.org/10.3847/1538-4357/aafd30

Magnetic Turbulence Spectra and Intermittency in the Heliosheath and in the Local Interstellar Medium

Federico Fraternale[1], Nikolai V. Pogorelov[2,4], John D. Richardson[3], and Daniela Tordella[1]
[1] Dipartimento di Scienza Applicata e Tecnologia, Politecnico di Torino, 10129, Torino, Italy; daniela.tordella@polito.it
[2] Department of Space Science, University of Alabama in Huntsville, Huntsville, AL 35805, USA
[3] Kavli Institute for Astrophysics and Space Research, Massachusetts Institute of Technology, Cambridge, MA 02139, USA
Received 2018 October 4; revised 2018 December 18; accepted 2018 December 19; published 2019 February 8

Abstract

The understanding of inertial-scale dynamics in the heliosheath is not yet thorough. Magnetic field fluctuations across the inner heliosheath (IHS) and the local interstellar medium (LISM) are here considered to provide accurate and highly resolved statistics over different plasma conditions between 88 and 136 au. By using the unique in situ 48 s measurements from the *Voyager Interstellar Mission*, we investigate different fluctuation regimes at the magnetohydrodynamic (MHD) scales, down to the MHD-to-kinetic transition. We focus on a range of scales exceeding five frequency decades ($5 \times 10^{-8} < f < 10^{-2}$ Hz), which is unprecedented in literature analysis. A set of magnetic field data for eight intervals in the IHS, in both unipolar and sector regions, and four intervals in the LISM is used for the analysis. Results are set forth in terms of the power spectral density, spectral compressibility, structure functions, and intermittency of magnetic field increments. In the heliosheath, we identify the energy-injection regime displaying a $\sim 1/f$ energy decay, and the inertial-cascade regime. Here, the power spectrum is anisotropic and dominated by compressive modes, with intermittency that can reach kurtosis values of up to 10. In the interstellar medium the structure of turbulence is anisotropic as well, with transverse fluctuations clearly prevailing after 2015 May. Here, we show that intermittent features occur only at scales smaller than 10^{-6} Hz.

Key words: ISM: kinematics and dynamics – magnetic fields – solar wind – Sun: heliosphere – turbulence – waves

1. Introduction

Voyagers 1 and 2 (*V*1 and *V*2) crossed the heliospheric termination shock (TS) in December 2004 and in 2007 August, respectively (Stone et al. 2005, 2008). It is widely accepted that on 2012 August 25, *V*1 crossed the heliopause (HP) and is now moving through the local interstellar medium (LISM; Burlaga et al. 2013b; Gurnett et al. 2013; Stone et al. 2013; Webber & McDonald 2013; Burlaga & Ness 2014a).

The magnetic field behavior beyond the HP is determined by the interstellar magnetic field (ISMF), which is draped over the HP as a tangential discontinuity that separates the solar wind (SW) from the LISM. The simulations of Pogorelov et al. (2009a, 2017b) and Borovikov & Pogorelov (2014) predicted a magnetic field behavior very similar to observations. The recent simulation of Kim et al. (2017) shows that the ISMF "undraping" is consistent with the time-dependent processes occurring in the SW. It also reproduces major shocks propagating through the LISM that cause the plasma wave events observed by the Plasma Wave Subsystem (PWS) between 2012 November and 2016 July (Gurnett et al. 2013, 2015; Pogorelov et al. 2017b). Interestingly, it also predicted a shock passing through *V*1 in 2017 August, when plasma waves were observed by the PWS. *V*2 remains in the inner heliosheath (IHS) and measures a velocity profile very different from that of *V*1 at the same distance from the Sun. It also gradually approaches the HP. Conventionally, the IHS is the SW region between the TS and the HP. The HP has structure that is clearly observed by *V*1. It was crossed in about one month, which gives a width of about 0.3 au. There are strong indications that this structure is due to the HP instability (Borovikov & Pogorelov 2014), magnetic reconnection (Schwadron & McComas 2013; Pogorelov et al. 2017b), or both.

Theoretical and numerical studies of the SW–LISM interaction have a long history that is reviewed, e.g., in Zank (1999, 2015), Izmodenov et al. (2009), Izmodenov & Alexashov (2015), Opher (2016), and Pogorelov et al. (2017a). The TS is formed due to deceleration of the supersonic wind when it interacts with the HP and LISM counterpressure. Modern models of the SW–LISM interaction take into account the effects of charge-exchange between ions and neutral atoms, coupling of the heliospheric magnetic field (HMF) and ISMF, and treat nonthermal (pickup) ions (PUIs) as a separate component (see Pogorelov et al. 2016, 2017b, and references therein).

As far as the model uncertainties are concerned, remarkably many observations of the SW/LISM bulk flow and average magnetic field have been reproduced by simulations. The deflection of the LISM neutral H atoms, e.g., is on average in the *BV*-plane, which is defined by the LISM velocity and ISMF vectors, $\boldsymbol{V}_\infty$ and $\boldsymbol{B}_\infty$, in the unperturbed LISM (Izmodenov et al. 2005; Pogorelov et al. 2008, 2009b; Katushkina et al. 2015). Kinetic energetic neutral atom (ENA) flux simulations of Heerikhuisen et al. (2010, 2014), Heerikhuisen & Pogorelov (2011), and Zirnstein et al. (2015a, 2015b, 2016, 2017, 2018) reproduced the *IBEX* ENA ribbon using the *BV*-plane consistent with the hydrogen deflection plane. A number of simulations reproduce *Voyager* measurements. Pogorelov et al. (2017b) demonstrated that the distribution of density in the heliospheric boundary layer (a region of decreased plasma density on the LISM side of the HP) is in agreement with PWS data. These models also reproduce the H density at the TS derived from PUI measurements (Bzowski et al. 2009) and observed anisotropy in the 1–10 TeV galactic cosmic ray flux

[4] Center for Space Plasma and Aeronomic Research, University of Alabama in Huntsville, Huntsville, AL 35805, USA.

(Schwadron et al. 2014; Zhang et al. 2014; Zhang & Pogorelov 2016).

Certain details in the observations and simulations clearly demonstrate that turbulence bears an imprint of physical processes occurring in the IHS and LISM. These are related to the turbulent character of the SW both in front of the TS and in the IHS, the presence of the heliospheric current sheet (HCS) that separates the sectors of opposite HMF polarity, the variability of the boundary between the sector and unipolar HMF, and the possibility that instabilities and magnetic reconnection destroy the HCS, thus resulting in the HMF decrease. In fact, simulations imply that turbulence may be affecting the interaction pattern by facilitating magnetic reconnection and instabilities. Moreover, the LISM turbulence may be affected by shocks propagating through it.

This paper is an attempt to address these issues by performing a turbulence analysis of *Voyager* data. In particular, this study provides a spectral characterization of the various regimes of magnetic field fluctuations from the energy-injection range (EI), through the inertial cascade (IC), down to scales where kinetic effects start to affect the dynamics ($\approx 10^4$ km). The analysis cannot be further extended to smaller scales due to resolution- and accuracy-related issues of *Voyager* data. However, it is known that the inertial-cascade regime of turbulence keeps track of physical processes taking place at smaller scales, which makes its analysis significantly intriguing.

HMF sectors in the IHS. A characteristic property of the SW flow is the existence of an HCS that separates magnetic field lines of opposite polarity, which originate at the solar surface. The HCS propagates with the SW kinematically, provided that it has no backreaction on the flow. Theoretical and numerical, kinetic and multi-fluid analyses of magnetic reconnection across the HCS have been discussed by Drake et al. (2010, 2017) and Pogorelov et al. (2013, 2017b). Magnetic reconnection may reveal itself as a tearing mode (or plasmoid) instability and may take place especially close to the HP, where the sector width decreases to negligible values.

The sectors of alternating magnetic field polarity in the IHS cannot be resolved. It is known that *V*1 had been observing a negative radial velocity component for two years before it crossed the HP (Pogorelov et al. 2009a, 2012; Decker et al. 2012). Because of the piling-up effect, the sector width should be negligible near the HP. Moreover, the sector width decreases to zero at the HCS tips, which makes attempts to resolve the traditional HCS structure very challenging. In addition, current sheets can be created not only due to the tilt of the Sun's magnetic axis, but also due to stream interactions that are abundant in the heliosphere. The transition to chaotic behavior of the HMF occurs when the sector width becomes smaller than the numerical resolution (Pogorelov et al. 2017b). In nature, this is possible both due to preexisting turbulence and magnetic reconnection across the current sheets, which also creates turbulence.

The approach followed by Borovikov et al. (2011) to track the HCS surface based on the assumption of HMF being unipolar is neither practical nor acceptable. Numerical simulations allow us to determine what happens to $\boldsymbol{B}$ if the HMF is assumed to be unipolar: it is clear that the calculated magnetic field strength in this case is substantially overestimated as compared with *V*1 observations in the IHS (see the discussions, e.g., in Pogorelov et al. 2015, 2017b). Thus, the possibility of HMF depressions in the IHS covered by a sectored HMF should not be disregarded. It can be identified by the increased turbulence level in relevant regions. *Voyager* spacecraft provide us with appropriate measurements to answer these questions.

Richardson et al. (2016) have investigated the effect of the magnetic axis tilt on the number of HCS crossings and compared the observed and expected numbers. It has been shown that the number of HCS crossings substantially decreased two years after *V*1 and *V*2 entered the IHS. However, *V*2 might have entered the unipolar region at that time. It was concluded that there are indications of magnetic field decrease possibly due to magnetic reconnection across the HCS. In addition, as shown by Drake et al. (2017), *V*2 data reveal that fluctuations in the density and magnetic field strength are anticorrelated in the sector regions, as is expected from their magnetic reconnection modeling, but not in the unipolar regions. A possible dissipation of the HMF in such regions may also be an explanation of a sharp reduction in the number of sectors, as seen from the *V*1 data.

Turbulence in the heliosheath and LISM. An extensive data analysis related to the SW turbulence behavior in the SW ahead of the TS and in the IHS along the *Voyager* trajectories was performed by Burlaga (1994), Burlaga et al. (2003a, 2003b, 2003c, 2006a, 2007), Burlaga & Ness (2009), and Burlaga et al. (2009, 2015, 2017, 2018). There is no single physical mechanism responsible for all observed turbulence manifestations. Large-amplitude fluctuations in the magnetic field strength B are observed at small scales with very complex profiles. These fluctuations were described as "turbulence" (Burlaga et al. 2006a; Fisk & Gloeckler 2008), although their nature and origin are not yet understood. The turbulence includes "kinetic scale" features (with sizes on the order of 10–100 gyroradii) and microscale features (>100 proton gyroradii). Usually, the observed turbulence consists of both coherent and random structures as seen in time profiles of the magnetic field strength on scales from 48 s to several hours. As shown by Burlaga et al. (2009), the large-scale (one day) fluctuations measured at *V*1 in the unipolar and sector regions differ in some aspects: they have a log-normal distribution in the post-TS region, but are Gaussian in the unipolar region. Instabilities and magnetic reconnection enhance turbulence, i.e., magnetic field dissipation in the sector region should naturally affect magnetic field and plasma density fluctuations inside the IHS.

Magnetic field fluctuations have als been observed in the LISM. However, these fluctuations are smaller than in the IHS (Burlaga et al. 2018), and their nature is not yet understood. In this paper, we investigate the LISM turbulence in different regions separated by shocks causing plasma wave emission observed by *V*1. Our methodology allows us to investigate these fluctuations in more detail than previously possible. In fact, as discussed in Section 2, an analysis of power spectra in the SW turbulence, which is necessary to address these issues, is a challenging task because of the sparsity of the 48 s data. After the TS, about 70% of the magnetic field 48 s data are missing. Thus, sophisticated spectral estimation techniques become mandatory for obtaining reliable and physically meaningful results.

In the present study, Section 2 describes the data sets used for the analysis. Section 3 contains results of the analysis of the IHS, and it is split in two parts: Section 3.1 for *Voyager* 2, and

Section 3.2 for *Voyager* 1. The LISM turbulence is discussed in Section 4, and final remarks follow in Section 5. In Appendix A, we report information of the methods used for spectral estimation. Finally, Appendix B, contains information on variance anisotropy.

2. *Voyager* Data in the IHS and LISM and Selected Periods

This study considers different intervals in the IHS and in the LISM. In particular, we used magnetic field data at the highest resolution publicly available, the 48 s averaged data measured in situ by the *Voyager Interstellar Mission* (https://voyager.jpl.nasa.gov/mission/interstellar-mission/). In the heliosheath and beyond, the *Voyager* LMF magnetometers (MAG experiment, see Behannon et al. 1977) sample the magnetic field at a rate of 2.08 samples per second. The rate of the telemetry is 0.0208 Hz, and 48 s averages are periodically published in the NASA Space Physics Data Facility (https://spdf.gsfc.nasa.gov/) and can also be accessed via the COHO website (https://cohoweb.gsfc.nasa.gov/coho/). Data are currently available through day-of-year (DOY) 271 of 2017 for *V*1, and through 2015 DOY 356 for *V*2, in *RTN* reference frame. The heliographic *RTN* coordinate system is centered at the spacecraft. The *R* axis points radially outward from the Sun, the *T* axis is parallel to the solar equatorial plane and points in the direction of the Sun's rotation, while the *N* axis completes the orthonormal triad. In the most sensitive LMF range, the level of noise is 0.006 nT. However, 1σ systematic errors due to the data calibration process and other sources of noise (sensors, electronics, telemetry system, and ground-tracking stations) are estimated around ± 0.02 and ± 0.03 nT at *V*1 and *V*2, respectively. Moreover, the variability of errors makes these uncertainties rise up to ± 0.1 nT in specific periods or for specific field components (Berdichevsky 2009). In addition to the noise, limited telemetry coverage (the Canberra antennas of the CDSCC can only view *V*1 and *V*2 12 hours per day) leads to data gaps of 8–16 hr per day. This point constitutes the major challenge for a spectral analysis, such as that presented for the first time in this study. The numerical techniques we used are synthetically described in Appendix A, and have previously been used in Fraternale et al. (2016), Gallana et al. (2016), and Fraternale (2017).

In the IHS we consider four periods for *V*1 and for *V*2, respectively, after 2009 (see Figure 1(a)). In particular, at *V*1 we selected the intervals (A1) 2009, DOY 22-2009, DOY 180 (109.5 ± 0.77 au); (B1) 2010, DOY 180-2011, DOY 180 (115.65 ± 1.79 au); (C1) 2011, DOY 180-2011, DOY 276 (117.91 ± 0.47 au); and (D1) 2011, DOY 276-2011, DOY 365 (118.81 ± 0.44). During these periods, *V*1 sampled almost unipolar magnetic fields with northern "toward" polarity with respect to the Sun. Periods C1 and D1 are separated by a sector boundary crossing that occurred in 2011, DOY 276, and lasted about one day, when the polarity became southern, "away," until 2012 DOY 209. During this period, interaction with the local interstellar plasma likely occurred. A detailed description of sector boundaries in proximity of the HP from 2011.5 can be found in Burlaga & Ness (2014b).

As the Plasma Science instrument is not operational at *V*1, the bulk wind speed can sometimes be recovered using a Compton–getting analysis from the low-energy charged particle experiment and cosmic ray subsystem data (Krimigis et al. 2011). The heliosheath plasma has been provided by Richardson & Burlaga (2013), Richardson & Decker (2014),

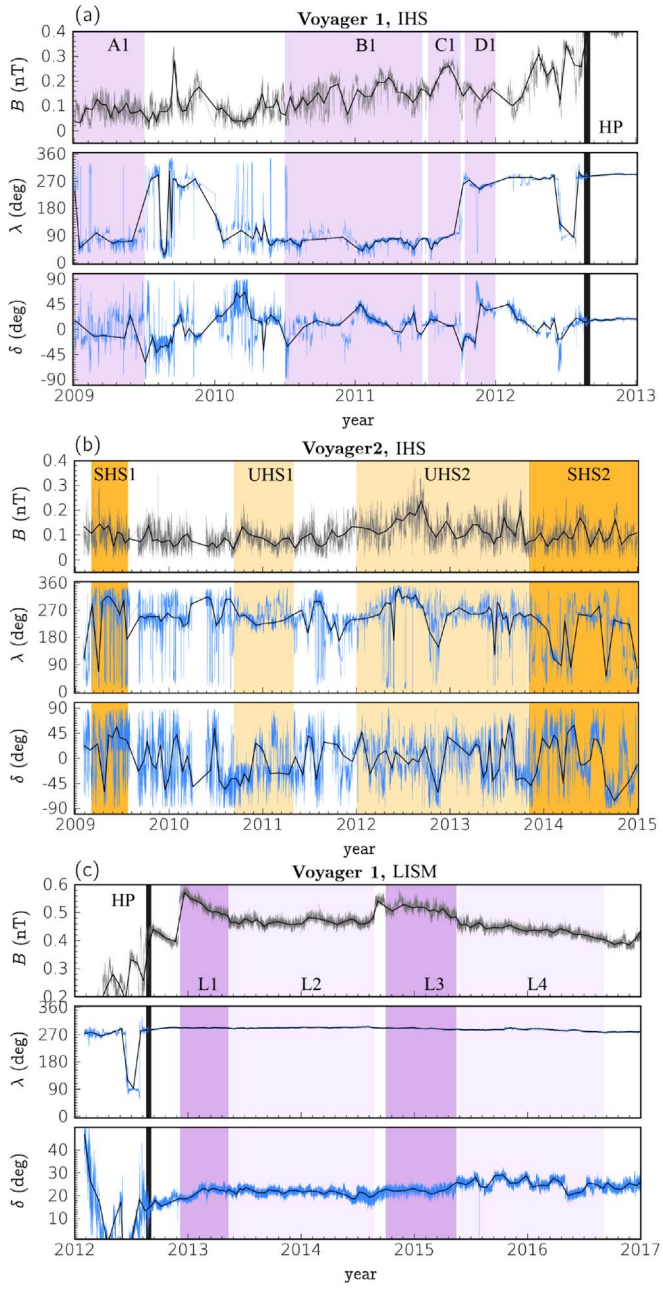

Figure 1. Data sets analyzed in this study. Top panels (a): *V*1, IHS. Middle panels (b): *V*2, IHS. Bottom panels (c): *V*1, LISM. Each panel contains from top to bottom the magnetic field magnitude, $B = |\boldsymbol{B}|$; the azimuthal angle, $\lambda = \tan^{-1}(B_T/B_R)$; and the elevation angle, $\delta = \sin^{-1}(B_N/B)$. Data points with $|B_{R,T,N}| < 0.03$ nT have not been used in the computation of λ and δ.

and Richardson & Decker (2015). For our analysis, it is particularly important to highlight that *V*1 (traveling at $V_{SC1} \approx 17\ \mathrm{km\ s^{-1}}$, 34°.5 North) measured low radial velocity components since its crossing the heliospheric TS. In particular, the radial velocity V_R decreased almost linearly from about $100\ \mathrm{km\ s^{-1}}$ (2006) to $0\ \mathrm{km\ s^{-1}}$ in 2010.5, while the tangential speed V_R oscillated around $-40\ \mathrm{km\ s^{-1}}$. Numerical simulations (Pogorelov et al. 2013) suggest that the absence of sector boundary crossings observed by *V*1 near the HP, as well as the negative radial velocity observed during 2011, could be a symptom of *V*1 being inside a magnetic barrier.

The flow at *Voyager* 2 ($V_{SC2} \approx 15\ \mathrm{km\ s^{-1}}$, 30° South) was quite different. The bulk speed remained almost constant at

about 150 km s^{-1} throughout the IHS. In contrast to *V*1 observations, high variability was found at *V*2 in the fluxes of energetic particles, as shown by Decker et al. (2008). This variability has been related to the possibility for *V*2 to be alternatively inside the unipolar region (UHS) or inside the sector region (SHS; Opher et al. 2011; Hill et al. 2014). The sector region is defined as the region swept by the HCS. Likely, *V*2 has been very close to the boundary between these two regions, according to models based on kinematic propagation of the maximal extension of the HCS, measured by the Wilcox Solar Observatory (http://wso.stanford.edu/). Richardson et al. (2016) compared the results of two models with the actual number of sector boundary crossings observed at *V*2. It is believed that the spacecraft remained in the unipolar region from 2009.5 until 2013.83 when it entered the sector region, as discussed by Burlaga et al. (2017).

Based on a literature analysis, we selected four intervals for *V*2, see Figure 1(b): (SHS1) 2009, DOY 62-2009, DOY 210 (89.0 ± 0.65 au); (UHS1) 2010 DOY 252-2011 DOY 210 (94.08 ± 1.89 au); (UHS2) 2012, DOY 1-2013, DOY 300 (100.20 ± 2.88 au); and (SHS2) 2013, DOY 300-2015, DOY 1 (104.95 ± 1.87 au). The thermal ion average plasma density (n_i) was about 0.001 cm^{-3} from 2009 to 2012, then increased to 0.002 cm^{-3} until 2015 (the standard deviation is 0.0007 in the last period and 0.0003 in the earlier periods). The thermal plasma temperature was 63,500 K in SHS1, 44,700 K in UHS1, 56,200 K in UHS2, and 51,700 K in SHS2 (with a standard deviation of about 22,000 K).

Ultimately, we considered four consecutive intervals of *V*1 data in the LISM, see Figure 1(c)): (L1) 2012, DOY 340-2013, DOY 130 (123.3 ± 0.77 au); (L2) 2013 DOY 133-2014 DOY 236 (126.4 ± 2.29 au); (L3) 2014 DOY 273-2015 DOY 135 (130.2 ± 1.11 au); and (L4) 2015 DOY 145-2016 DOY 246 (133.7 ± 2.28 au). This partition was also identified by Burlaga & Ness (2016): in that study, L1 and L3 were referred to as "disturbed" intervals and L2 and L4 as "quiet." The periods L2 and L4 have also been considered by Burlaga et al. (2015, 2018, respectively). These regions are bounded by weak perpendicular shocks (or pressure waves) propagating through the LISM, as shown by Burlaga et al. (2013a), Gurnett et al. (2013, 2015), Burlaga & Ness (2016), and Kim et al. (2017). The interstellar plasma is colder than the IHS ($T \approx 10^4$ K). Electron plasma oscillations detected by *V*1's PWS yielded a density estimate of 0.08 cm^{-3} (Gurnett et al. 2013). These oscillations are driven by electron beams produced upstream of the shocks. Until 2016, five events have been detected (2012 October–November, 2013 April–May, 2014 February–November, and 2015 September–November).

In this study, we removed outliers from the 48 s data sets. This was done by computing a backward- and forward-moving variance over a 48 hr window (3600 data points). For each magnetic field component, a data point was removed if it was larger than six times the minimum between the backward- and the forward-moving standard deviation ($|B_j| > 6 \min\{\sigma_{b_j}, \sigma_{f_j}\}$, $j = 1,...,n$). Moreover, three calibration events (spacecraft rolls with 30-minute periodicities) were removed from intervals A1 and SHS1. Magnetic field data have been rotated to mean field coordinates: a *B*-parallel component $B_\parallel$, and two perpendicular components $B_{\perp 1}$, $B_{\perp 2}$ with respect to the average field $\boldsymbol{B}_0$, which better suits the turbulence analysis ($B_{\perp 1}$ is in the *T*–*N* plane and $B_{\perp 2}$ completes the right-handed triplet). Since the SW flow and the magnetic field directions in the IHS are nearly orthogonal, $B_\parallel \approx B_T$, $B_{\perp 1} \approx B_N$, and $B_{\perp 2} \approx B_R$. Moreover, we removed linear trends for each component.

In the following, letters in bold indicate vector fields and standard letters are used for the magnitude of vector fields.

3. Magnetic Field Fluctuations in the IHS

This section shows the results of the magnetic field fluctuation analysis in the IHS. We provide a spectral analysis for a frequency range wider than five decades, $f \in [10^{-8}, 10^{-2}]$ Hz. Before we discuss the results, we introduce some definitions and symbols.

We computed the power snels of Figpectral density (PSD, or *P*), shown in Figures 2, and 5 for the IHS and in the left paure 7 for the LISM. Due to the issue of the missing data, the PSD is estimated via three different numerical procedures (Appendix A). The comparative analysis of these techniques allows us to recover the PSD with an uncertainty of the spectral indexes that is typically smaller than 10%.

We investigated the spectral compressibility and variance anisotropy (Figures 3, 8, 10, 11, and 12). The anisotropy is expressed in terms of both $P[B_j]/E_m$ ($j = \{\parallel, \perp_1, \perp_2\}$) and $P[B_\perp]/P[B_\parallel]$, where $P[B_\perp] = P[B_{\perp 1}] + P[B_{\perp 2}]$. Due to the lack of accurate plasma data, we use the ratio between the PSD of the field magnitude and the trace as a proxy for the spectral compressibility: $C(f) = \mathrm{P}[B]/E_\mathrm{m}$, where $E_\mathrm{m}(f) = \mathrm{tr}(\mathrm{P}[\boldsymbol{B}]) = \mathrm{P}[B_\parallel] + \mathrm{P}[B_{\perp 1}] + \mathrm{P}[B_{\perp 2}]$. This measure is an index of the alignment of the fluctuation vector with the average field. Fluctuations of the magnetic field magnitude can indeed be considered as a proxy for density fluctuations to a good degree of approximation. In fact, strong correlations between plasma density and $|\boldsymbol{B}|$ have been found in both rarefaction and compression regions between 1 and 11 au by Roberts et al. (1987). Similar correlations have also been found previously by Smith et al. (1983) and Goldstein et al. (1983). We also computed the fraction of parallel energy in the time domain via two slightly different formulas:

$$C_1 = \left\langle \left(\frac{\boldsymbol{B}_0 \cdot \boldsymbol{\delta B}}{B_0 \delta B} \right)^2 \right\rangle, \quad C_2 = \frac{\langle (\boldsymbol{b} \cdot \boldsymbol{\delta B})^2 \rangle}{\langle \delta B^2 \rangle}. \tag{1}$$

In the above expressions, $\delta\boldsymbol{B} = \boldsymbol{B} - \boldsymbol{B}_0$ is the three-dimensional fluctuation about the background field, $\delta B = (\delta B_\parallel^2 + \delta B_{\perp 1}^2 + \delta B_{\perp 2}^2)^{1/2}$ is its magnitude, and $\boldsymbol{b} = \boldsymbol{B}_0/B_0$ is the direction cosines vector. Angle brackets indicate the ensemble average over all the data points of each interval, and the dot indicates the scalar product. The powers of 2 used in Equation (1) allow us to interpret C1 and C2 as the average percentage of the fluctuating energy in the direction of $\boldsymbol{B}_0$. To reduce the contribution of noise, the computation is performed with hourly averaged data. Compressibility values are reported in Tables 2, 4 (IHS), and 5 (LISM). It should be noted that for a fluctuating field with constant magnitude and isotropic angle distribution, $C = 0.33$.

These tables also report information on other fluctuation properties such as the average turbulence intensity,

$$I = \left\langle \left| \frac{\delta B}{B_0} \right| \right\rangle, \quad I_j = \left\langle \left| \frac{\delta B_j}{B_0} \right| \right\rangle, \quad j = \{\parallel, \perp_1, \perp_2\}, \tag{2}$$

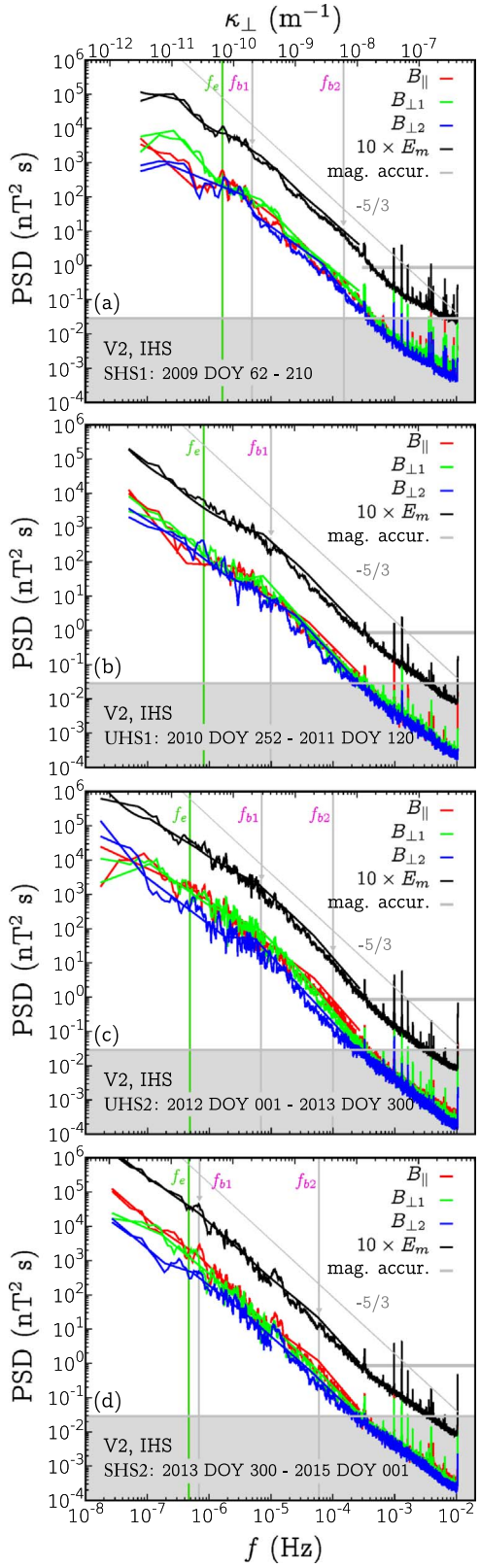

Figure 2. Power spectral density of magnetic field fluctuations at *Voyager* 2 in the IHS. For clarity, the trace (E_m) has been magnified by a factor of 10. Details about the methods for spectral estimation are given in Appendix A.

the maximum-variance fluctuation amplitude ($\delta B_{\rm mv}$) and direction with respect to B_0 ($\theta_{\rm mv}$), spectral breaks and spectral indexes, and power-law exponents for the structure functions.

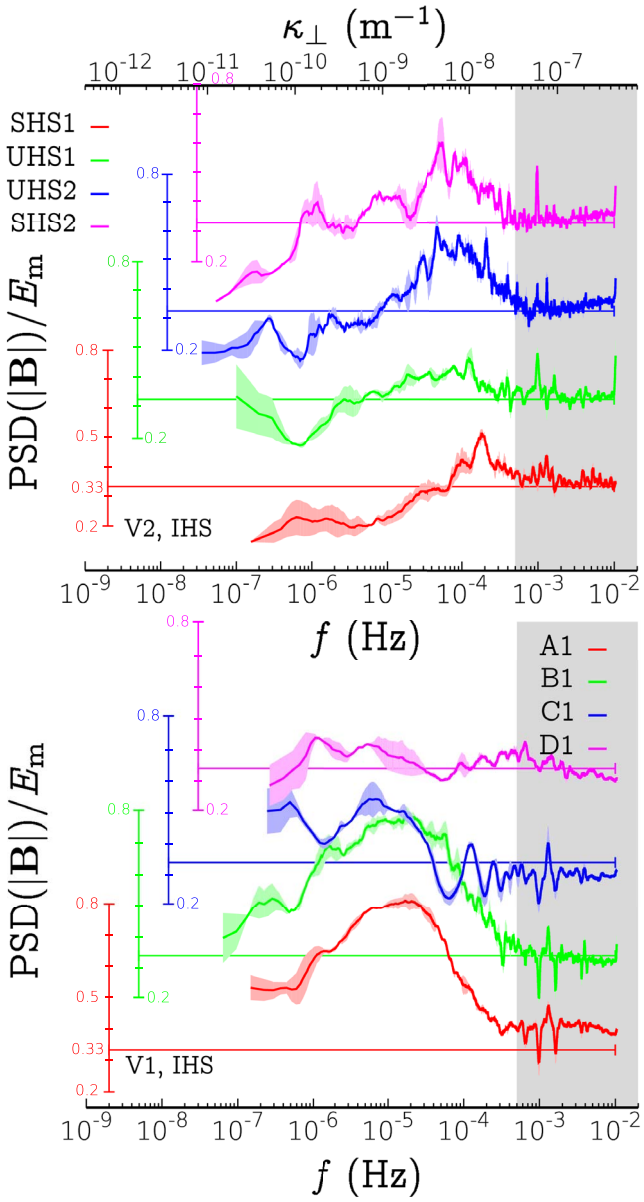

Figure 3. Spectral compressibility in the IHS at *Voyager* 2 (top panel) and *Voyager* 1 (bottom). The colored areas show the variability due to the methods we used for the computation of the spectrum (see Appendix A). Average values computed through Equation (1) are shown in Tables 2 and 4 for *V*2 and *V*1, respectively.

In fact, we performed a multiscale analysis of the magnetic field increments via computation of the structure functions $S_p(f)$, a classical and powerful statistical tool for investigating the departure from self-similarity and the intermittent behavior of turbulence (Monin & Yaglom 1971; Frisch 1995; Politano & Pouquet 1995; Politano et al. 1998),

$$S_{p,j}(\tau) = \langle |B_j(t) - B_j(t+\tau)|^p \rangle, \; j = \{\parallel, \perp_1, \perp_2\}. \qquad (3)$$

We used the absolute values in this definition for better convergence of statistics for the odd moments. The computation of $S_{p,j}$ from discrete data is nontrivial for *Voyager* data sets due to the amount and distribution of missing data. For this computation, we did not interpolate data and computed the

statistics for the ensemble of available differences:

$$S_{pj}(\tau_k) = \frac{1}{N(\tau_k)} \sum_{i=1}^{N(\tau_k)} |B_j(t_i) - B_j(t_i + \tau_k)|^p,$$
$$\tau_k = k \cdot \Delta t_s \quad k = 1, \ldots, n \tag{4}$$

where Δt_s is the data resolution and n the total number of points of the data set (we used both 48 s data and 1824 s averages). The counter $N(\tau_j)$ of decreases with τ and also depends on the distribution of missing data. The amount of missing data is between 55% (A1) and 80% (D1), and the dominant periodicity of the data gaps is 43000 s ± 2000 s ($f_{\rm gap} = 2.3 \times 10^{-5} \pm 10^{-6}$ Hz). From the structure functions, one computes the scale-dependent kurtosis of magnetic field increments, which is an indicator of intermittency:

$$K(\tau) = \frac{S_4(\tau)}{S_2^2(\tau)}. \tag{5}$$

Structure functions and kurtosis are shown in Figures 4 and 6 for the IHS, and in Figure 7 for the LISM.

The spectra computed from in situ single-spacecraft measurements are inevitably 1D-reduced spectra (Matthaeus & Goldstein 1982) with frequencies measured in the spacecraft reference frame ($f_{\rm SC}$). The Doppler-shift relationship between the spacecraft and the plasma reference frame ($f_{\rm PL}$) reads

$$f_{\rm SC} = f_{\rm PL} + (2\pi)^{-1} \boldsymbol{k} \cdot \boldsymbol{V}_{\rm rel}, \tag{6}$$

where $\boldsymbol{k}$ is the vector wavenumber and $\boldsymbol{V}_{\rm rel} = \boldsymbol{V}_{\rm SW} - \boldsymbol{V}_{\rm SC}$ the relative speed between the spacecraft and the plasma flow across it. Note that for an Alfvénic nondispersive large-scale wave, the maximum value is reached for parallel fluctuations, $f_{\rm PL} = \kappa_\parallel V_{\rm A}/2\pi$. For dispersive waves, instead (as in the kinetic regime), $f_{\rm PL}$ is typically a function of higher powers of the wavenumber. If $f_{\rm PL} \ll |\boldsymbol{\kappa} \cdot \boldsymbol{V}_{\rm rel}|/2\pi$ (Taylor's hypothesis, Taylor 1938, see also the discussion in Howes et al. 2014), frequencies measured at the spacecraft can be converted into wavenumbers in the direction of the relative wind flow. In the SW, this condition is satisfied on large scales as the flow is super-Alfvénic and the spacecraft is slow compared with the wind. This condition typically holds for the SW upstream of the TS, where $V_{\rm SC}/V_{\rm SW} \lesssim 0.05$. In the IHS, the situation is quite different at *V*1 and *V*2. At *V*2, in fact, $V_{\rm SC}/V_{\rm SW} \approx 0.1$ and $V_{\rm A}/V_{\rm SW} \approx 0.3$. The $B - V$ angle is nearly equal to $\pi/2$, and Taylor's approximation might be used to obtain perpendicular wavenumbers, $\kappa_\perp \approx 2\pi f_{\rm SC2}/V_{\rm SW}$. We report the wavenumber value in all *V*2 figures. We recall, however, that reduced spectra always contain contributions from all vector wavenumbers.

At *V*1, given that the spacecraft was in the slow-wind region, Taylor's approximation does not hold.

While performing the turbulence analysis of SW fluctuations, it is important to consider the causality condition. In fact, a fluctuation (or "eddy") with typical velocity scale δv and size ℓ experiences one "eddy turnover" in a period $t \sim \pi\ell/\delta v$. During this period, the eddy is convected by the wind by a distance equal to $d = V_{\rm SW} t$. Assuming the frozen-flow approximation, this fluctuation would be detected by the spacecraft at a frequency $f_{\rm e} \approx \kappa V_{\rm SW}/2\pi \approx V_{\rm SW}/\ell \approx \pi V_{\rm SW}/(\delta v t) \approx \pi V_{\rm SW}^2/(\delta v\ d)$. Recalling that d is the distance traveled by the eddy from its origin to the spacecraft, one obtains $f_{\rm e} \approx \pi V_{\rm SW}^2/[\delta v\ (r_{\rm SC} - r_{\rm source})]$. Eventually, considering $\delta v \approx V_{\rm A}$, the following expression is obtained

$$f_{\rm e} \approx \frac{\pi V_{\rm SW}^2}{V_{\rm A}(r_{\rm SC} - r_{\rm source})}. \tag{7}$$

This means that frequencies lower than $f_{\rm e}$ in the spacecraft reference frame correspond to structures that did not yet experience one eddy-turnover, or equivalently, waves that do not satisfy the causality condition, because they would have traveled from a farther distance than their source point. In the SW upstream of the TS, the Sun can be clearly considered as the source point. In this case, fluctuations with $f_{\rm SC} \lesssim f_{\rm e}$ would be older than the age of the plasma. Fluctuations with $f_{\rm SC} \gtrsim f_{\rm e}$ instead can be considered "active" fluctuations, meaning that they may be part of a turbulent energy cascade.

In this study, we computed $f_{\rm e}$ only at *V*2 and considered the TS as the source location.

Due to the differences highlighted above between the plasma flow at the two spacecraft and their spatial and temporal separation, magnetic field fluctuations in the IHS at *V*2 and *V*1 are discussed in two separate subsections, Sections 3.1 and 3.2, respectively.

3.1. IHS Analysis of Voyager 2 Data

Figure 2 shows magnetic field power spectra of the four selected periods of *V*2 data. The average plasma parameters are summarized in Table 1. Information about the average fluctuating energy, compressibility, and strength of fluctuations is reported in Table 2, together with the frequency of spectral breaks and power-law exponents. Different regimes are identified.

Let us start the discussion with the high-frequency range ($10^{-3} \lesssim f < 10^{-2}$ Hz). In principle, 48 s data could allow us to investigate the beginning of the kinetic regime, as the ion cyclotron frequency in the IHS is on the order of mHz (see Smith et al. 2006a; Alexandrova et al. 2008, 2012, and Schekochihin et al. 2009 for a detailed review). Unfortunately, however, noise affects the data, as explained in Section 2. Thus, all PSD figures contain a gray band at a power level of $P_{\rm noise} = 0.029$ nT^2 s, corresponding to a white noise of 0.03 nT amplitude (the actual distribution of the noise is unknown, this is a conservative threshold). The band is set at $P_{\rm noise} = 0.086$ nT^2 s for $E_{\rm m}(f)$. The noisy region includes frequencies $f \gtrsim 5 \times 10^{-4}$ Hz. Here, a spectral flattening toward a -1 spectral slope is observed, together with some instrument-related spikes and harmonics of the sampling rate. Note, however, that the spectral profiles do not correspond to white noise, and that in the last frequency decade, the spectra show definite trends and retain some information on the anisotropy. Moreover, these trends are not strictly identical among data sets (see, e.g., the flattening and consecutive steepening at *V*1 during A1 in Figure 5(a)). Taking as an example SHS1, the flattening starts around $f > 10^{-3}$ Hz, where $P < 4 \times 10^{-3}$ nT^2 s. Tests show that this may be due to white noise with an amplitude 0.005 nT and standard deviation 0.003 nT (Gallana et al. 2016). This seems to suggest that the actual noise level is below the estimates, at least during some periods, and physical results may still be detectable (note that a similar issue occurred for *Voyager* velocity measurements in Roberts et al. 1987). Thus, we show PSDs for the full range of frequencies up to the Nyquist frequency for the 48 s resolution. The uncertainty bands reported here should be considered as upper bounds for the spectral region that may be affected by the noise.

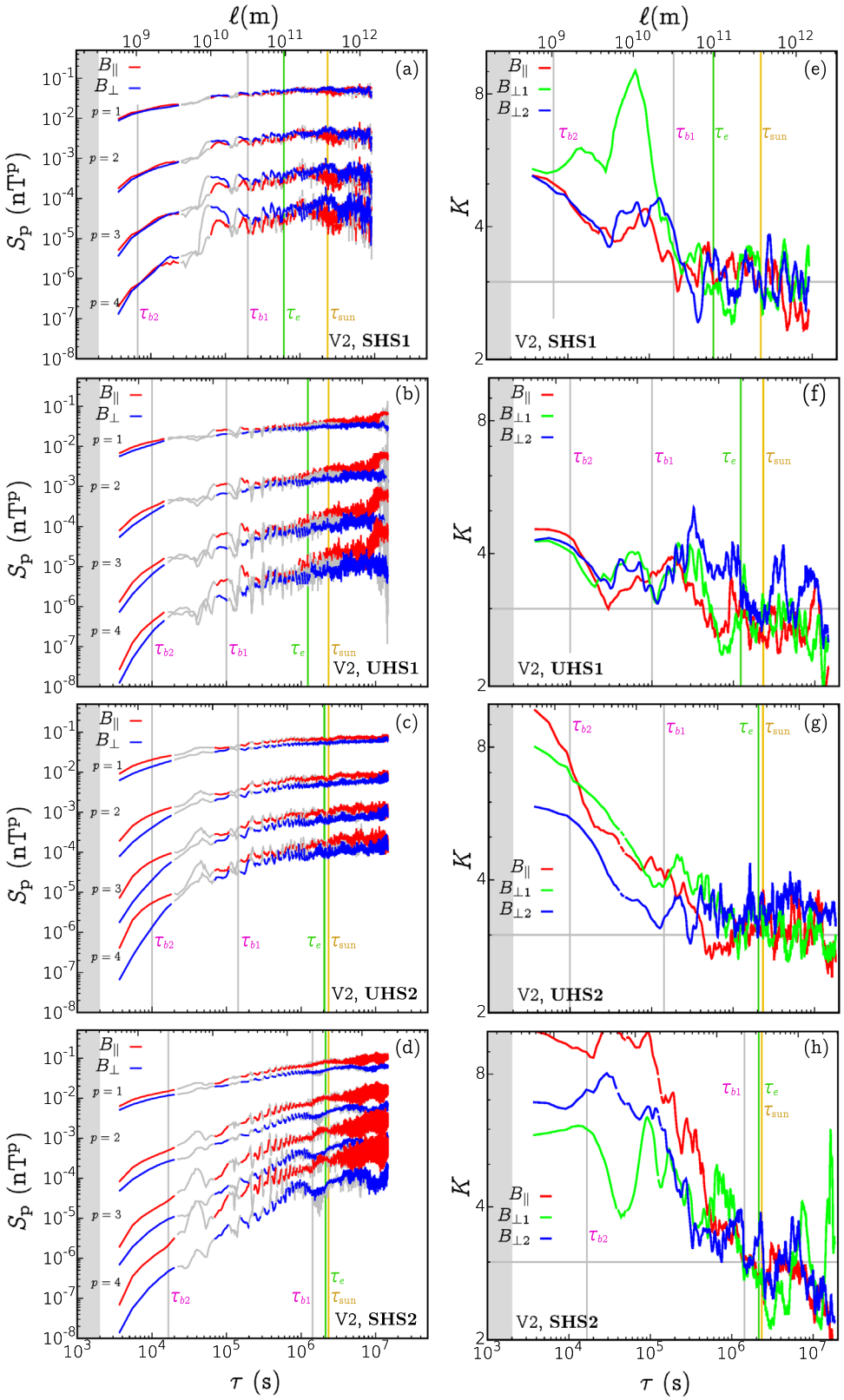

Figure 4. Structure functions and intermittency at *Voyager* 2 in the IHS. Left panels (a)–(d): Structure functions of B-parallel fluctuations, $S_{p,\parallel}$ (red curves), and B-perpendicular fluctuations $S_{p,\perp} = (S_{p,\perp 1} + S_{p,\perp 2})/2$ (blue curves). The timescales of spectral breaks (see Figure 2), τ_{b1} and τ_{b2}, are indicated with gray vertical lines. Timescales corresponding to the solar rotation, τ_{Sun}, and $\tau_e = 1/f_e$, are also shown. Right panels (e)–(h): Kurtosis of magnetic field increments, obtained via Equation (5).

Moreover, the cyclotron frequency of low-energy PUIs (1 keV) falls within this range, as shown in Table 1. It would be interesting to investigate the effect of PUIs in mediating turbulence and driving kinetic waves, which can affect the high-frequency part of the inertial regime, as shown in Smith et al. (2006b), Cannon et al. (2014a, 2014b), and Aggarwal

Table 1
Averaged Quantities at *Voyager* 2 in the IHS

Voyager 2	SHS1	UHS1	UHS2	SHS2
r_{SC} (au)	89.0	94.1	100.2	104.9
V_0 (km s^{-1})	157	151	154	153
B_0 (nT)	0.062	0.072	0.090	0.030
B (nT)	0.096	0.086	0.128	0.100
n_p (cm^{-3})	1.1×10^{-3}	1.0×10^{-3}	1.9×10^{-3}	1.8×10^{-3}
T_p (10^4 K)	6.35	4.47	5.63	5.17
V_A (km s^{-1})	63.4	59.2	63.9	51.6
β_p	0.54	0.46	0.54	1.00
$\beta_{p\ 1\ keV}$	19.6	24.3	22.2	45.0
r_{ip} (km)	6852	7186	5214	5357
r_{cp} (km)	3502	3301	2485	3038
$r_{cp\ 1\ keV}$ (km)	53000	53165	35695	45480
$f_{ip\ SC}$ (mHz)	11.5	10.5	14.8	14.3
f_{cp} (mHz)	1.47	1.31	1.95	1.15
$f_{cp\ SC}$ (mHz)	22.4	22.8	30.9	25.2
$f_{cp\ 1\ keV\ SC}$ (mHz)	1.65	1.42	2.16	1.68
f_e (Hz)	1.6×10^{-6}	8×10^{-7}	4×10^{-7}	4.5×10^{-7}

Note. Plasma quantities are computed from PLS data available in the NASA COHO website. The table reports r_{SC}, the Sun-*V*1 distance; $V_0 = (V_{0R}^2 + V_{0T}^2 + V_{0N}^2)^{1/2}$ and B_0, the magnitudes of the average velocity and magnetic field, respectively; and B, the average magnetic field strength. For the thermal protons: f_{cp}, the cyclotron frequency; n_p, the average density; T_p, the average temperature; V_A, the Alfvén velocity; $\beta_p = \langle 2\mu_0 n_p k_B T_p / B^2 \rangle$, the beta of thermal ions; $\beta_{p\ 1\ keV}$, the beta of 1 keV PUIs ($n_{1\ keV} \approx 0.2\, n$); r_{ip}, the ion inertial radius; and r_{cp}, the gyroradius. $r_{cp\ 1\ keV}$ is the ion gyroradius of a 1 keV pickup proton. Via Taylor's approximation, frequencies are also converted in the spacecraft reference frame $f_{SC} \approx V_{SW}/(2r)$. Finally, the one-eddy-turnover frequency f_e is shown (Equation (7)).

et al. (2016) for the SW from 1 to 6 au. In fact, in the IHS, the pickup-ion effect is expected to be considerable because the density of 1–5 keV pickup protons is about 20% of the thermal protons density (Zank et al. 2010).

At larger scales, most spectra show the presence of a low-frequency regime ($f \lesssim 10^{-5}$ Hz), which we interpret as the EI, a reservoir of energy for turbulence. Here, the magnetic energy decays as $1/f$. In particular, the spectral index α_1 falls between 0.7 and 1.3 for all the components. We computed the spectral index by linear regression in the log–log space. The uncertainty due to the fit is always much smaller than that related to the different spectral estimation techniques. Errors are shown in Table 2; they are usually larger in the EI range.

Interestingly, a spectral break (f_{b1}) characterizes the end of the EI range and the beginning of a steeper cascade, which is interpreted as the IC of turbulence. The spectral break between the EI and the IC regimes and the large-scale $\sim 1/f$ power law are known to exist in the SW upstream of the TS (the first observation was reported by Tu et al. 1984). Roberts (2010) investigated this regime with a focus on the effect of radial distance and cross-helicity for both fast, Alfvénic, and slow, less Alfvénic, regions from 0.3 to 5 au. In Alfvénic regions out to 5 au, the *Ulysses* study showed that f_{b1} is between 10^{-5} and 10^{-4} Hz (Bruno et al. 2009; Roberts 2010). In non-Alfvénic regions, the exact location is less clearly determined and is still a current topic of interest (Bruno et al. 2018).

Interpretations of the nature of this regime include the superposition of uncorrelated samples of solar surface turbulence having log-normal distributions of correlation lengths (Matthaeus & Goldstein 1986) that can determine $1/f$ energy decay (Montroll & Shleisinger 1982), and the reflection of primarily outward-traveling Alfvén waves in presence of large-scale inhomogeneities (Velli et al. 1989; Perez & Chandran 2013; Tenerani & Velli 2017).

In the IHS, a $1/f$ energy decay was observed at *V*1 during 2009 by Burlaga & Ness (2012) via multi-fractal analysis. Their observations were limited to the range $f \in [10^{-7}, 10^{-5}]$ Hz, which did not allow them to investigate the existence and location of spectral breaks in the IHS, shown here for the first time (the only power spectra in the IHS published so far are shown in Burlaga & Ness 2010, 2012, 2014b).

Figure 5 and Table 2 show that at *V*2 the break frequency f_{b1} observed in $E_m(f)$ (black curves) is about 5×10^{-5} Hz for SHS1, corresponding to a spatial scale $\ell_{b1} \approx 0.2$ au along the wind direction. Considering the age of fluctuations that originate at the Sun, one obtains from Equation (7) a cutoff frequency of 10^{-8} Hz. The actual break is instead more consistent with f_e of fluctuations generated at the TS (or affected by it). Moreover, it is not physically reasonable to consider turbulent structures with sizes greater than the outer scale of the system. The IHS width observed by *V*1 is around 27 au, corresponding to $\kappa \approx 1.5 \times 10^{-12}$ m^{-1} (note the wavenumber axis $\kappa \sim \kappa_\perp$ in all *V*2 plots). Moreover, solar rotation acts as a forcing with $f_{Sun} \approx 4 \times 10^{-7}$ Hz. The sector spacing should be around 2 au after TS and decrease as the HP is approached, even though the canonical sector structure is no longer recognizable beyond 10 or 20 au.

It seems that f_{b1} increases in the unipolar periods UHS1 and UHS2 to values around 10^{-5} Hz ($\ell_{b1} \approx 0.1$ au), while it decreases again to $f_{b1} \approx 7 \times 10^{-7}$ Hz ($\ell_{b1} \approx 1.5$ au) in the sectored interval SHS2, where the break is actually very weak. Note also that the break location differs for the $\delta B_\parallel$, $\delta B_{\perp 1}$, and $\delta B_{\perp 2}$ components, which are represented by the red, green, and blue curves, respectively, in Figure 2. In fact, the break of the *B*-perpendicular fluctuations occurs at a higher frequency than in the *B*-parallel one, by a factor between 2 and 7 for all periods except for the last one. We cannot be sure because of the noisy plasma data, but unipolar regions are at least initially much more Alfvénic (and thus have higher f_{b1}) than sector regions, and this might account for the differences seen here between the sectored and unipolar regions.

The high slope in the power spectra at $f \gtrsim f_{b1}$ suggests that a turbulent IC is ongoing. Moreover, in all intervals except for UHS1, a second spectral knee is observed at $f_{b2} \approx 10^{-4}$ Hz ($\ell_{b2} \approx 0.01$ au). It is particularly visible in the $B_\parallel$ component, while it is weaker and not always observed in $B_\perp$. The spectral slope between the two breaks, α_2, is about -1.6 for SHS1 and SHS2, which is close to the Kolmogorov $-5/3$ value (Kolmogorov 1941) and compatible with the model of Goldreich & Sridhar (1995, 1997) for the *k*-perpendicular cascade of critically balanced turbulence. The latter model, however, is not quite adequate because it ignores the compressibility, which plays a fundamental role in heliosheath and interstellar turbulence.

During unipolar periods the magnetic energy decays slightly faster and the index is around -1.75. Note that in general, the perpendicular components contribute to the steepening of the spectra, and that the UHS2 spectrum changes slope in rather a continuous way across frequencies. Beyond f_{b2}, the slope increases to $\alpha_3 \approx -2$. The cyclotron frequency of thermal

Table 2
Magnetic Field Fluctuation Properties at *V2* in the IHS

Voyager 2	SHS1	UHS1	UHS2	SHS2
E_m (nT^2)	6.76×10^{-3}	3.42×10^{-3}	1.17×10^{-2}	1.18×10^{-2}
C_2	0.29	0.42	0.35	0.43
C_2	0.35	0.63	0.48	0.64
$I_\parallel$	0.50	0.45	0.52	2.29
$I_{\perp 1}$	0.62	0.37	0.50	2.14
$I_{\perp 2}$	0.44	0.25	0.49	1.06
I	1.04	0.74	1.00	3.70
$\delta B_{\rm mv}$	0.051	0.043	0.067	0.088
$\theta_{\rm mv}$	106°	153°	86°	51°
$f_{\rm b1}$ (Hz)	5×10^{-6}	10^{-5}	7×10^{-6}	7×10^{-7}
$f_{\rm b2}$ (Hz)	2×10^{-4}	⋯	10^{-4}	7×10^{-5}
α_1	-0.98 ± 0.10	-1.10 ± 0.03	-1.18 ± 0.05	-1.25 ± 0.13
α_2	-1.64 ± 0.01	-1.78 ± 0.06	-1.78 ± 0.13	-1.58 ± 0.02
$f_{\rm b1,\parallel}$ (Hz)	2×10^{-6}	3×10^{-6}	2×10^{-6}	7×10^{-7}
$f_{\rm b2,\parallel}$ (Hz)	2×10^{-4}	10^{-4}	5×10^{-5}	6×10^{-5}
$\alpha_{1,\parallel}$	-0.74 ± 0.10	-0.97 ± 0.12	-0.84 ± 0.05	-1.15 ± 0.02
$\alpha_{2,\parallel}$	-1.62 ± 0.02	-1.60 ± 0.10	-1.34 ± 0.05	-1.57 ± 0.03
$\alpha_{3,\parallel}$	-1.97 ± 0.02	⋯	-2.08 ± 0.02	-2.02 ± 0.08
$f_{\rm b1,\perp}$ (Hz)	5×10^{-6}	2×10^{-5}	8×10^{-6}	7×10^{-7}
$f_{\rm b2,\perp}$ (Hz)	2×10^{-4}	⋯	⋯	7×10^{-5}
$\alpha_{1,\perp}$	-0.80 ± 0.10	-1.25 ± 0.04	-1.13 ± 0.03	-1.11 ± 0.10
$\alpha_{2,\perp}$	-1.64 ± 0.02	-1.87 ± 0.06	-2.05 ± 0.05	-1.58 ± 0.02
$\alpha_{3,\perp}$	-1.70 ± 0.05	⋯	⋯	-1.70 ± 0.05
$\zeta_{1,\parallel}$ ($\zeta^{\rm ess}_{1,\parallel}$)	0.33 (**0.35**)	0.30 (**0.33**)	0.28 (**0.41**)	0.40 (**0.41**)
$\zeta_{2,\parallel}$ ($\zeta^{\rm ess}_{2,\parallel}$)	0.67 (**0.68**)	0.57 (**0.67**)	0.48 (**0.74**)	0.75 (**0.75**)
$\zeta_{3,\parallel}$ ($\zeta^{\rm ess}_{3,\parallel}$)	1.02 (1)	0.82 (1)	0.67 (1)	1.05 (1)
$\zeta_{4,\parallel}$ ($\zeta^{\rm ess}_{4,\parallel}$)	1.38 (**1.30**)	1.04 (**1.31**)	0.89 (**1.20**)	1.31 (**1.18**)
$\zeta_{1,\perp}$ ($\zeta^{\rm ess}_{1,\perp}$)	0.40 (**0.37**)	0.25 (**0.34**)	0.37 (**0.38**)	0.33 (**0.36**)
$\zeta_{2,\perp}$ ($\zeta^{\rm ess}_{2,\perp}$)	0.82 (**0.71**)	0.45 (**0.67**)	0.62 (**0.71**)	0.62 (**0.70**)
$\zeta_{3,\perp}$ ($\zeta^{\rm ess}_{3,\perp}$)	1.25 (1)	0.64 (1)	0.81 (1)	0.87 (1)
$\zeta_{4,\perp}$ ($\zeta^{\rm ess}_{4,\perp}$)	1.69 (**1.24**)	0.82 (**1.30**)	0.98 (**1.26**)	1.10(**1.25**)

Note. All quantities are defined in Section 3.1. Spectral breaks and indexes of perpendicular fluctuations refer to the total power spectrum $P[B_\perp] = P[B_{\perp 1}] + P[B_{\perp 2}]$.

protons, $f_{\rm cp}$, is around 2 mHz (see Table 1). Moreover, structures with the size of the Larmor radius convected across the spacecraft may affect the power spectra at spacecraft-frame frequencies close to $f_{\rm cp\ SC} \approx 10^{-2}$ Hz. Structures with a size comparable with the ion inertial radius should similarly be detected at $f_{\rm ip\ SC} \approx 2.5 \times 10^{-2}$ Hz. In all likelihood, the second break $f_{\rm b2}$ is still within the magnetohydrodynamic (MHD) inertial range. However, we suggest that gyroradii of 1 keV PUIs may affect the turbulence at $f_{\rm cp\ 1\ keV\ SC} \approx 10^{-3}$ Hz (this frequency shifts to lower values as $E(\rm eV)^{-1/2}$). We see that a reduction of compressibility and intermittency takes place in the range $f_{\rm b2} \lesssim f \lesssim 10^{-3}$ Hz .

To simplify comparisons and prevent misunderstandings, we emphasize that our $P[B_{\perp 1}]$ is sometimes referred to as the "perpendicular spectrum," whereas $P[B_{\perp 2}]$ corresponds to the "quasi-parallel" spectrum (Matthaeus et al. 1990; Bieber et al. 1996). The ratio of these two spectra is equal to 1 in the case of pure slab turbulence and 1.67 in the case of pure 2D turbulence. The slab/2D model is not descriptive of the IHS or LISM turbulence because it ignores compressible fluctuations.

The spectral compressibility is shown in Figure 3 (top panel), while the variance anisotropy is shown in Appendix B (Figure 10). It is seen that the magnetic field fluctuations are primarily transverse in the EI range. At the beginning of the IC regime, $P[B_\perp]/P[B_\parallel] \approx 2$, meaning that $\delta B_\parallel$ accounts for ∼30% of the energy, and it approaches unity at $f_{\rm b2}$, where maximum compressibility is indeed observed (∼50% of the energy in $\delta B_\parallel$). These values of compressibility are relatively high when compared to near-Earth SW. The present IHS observations seem consistent with those by Smith et al. (2006b) from *ACE* observations at 1 au if we take the large β_p that is due to the PUI population into account.

The existence of a turbulent inertial range is further investigated by analyzing the structure functions of temporal increments in the magnetic field, $S_p(\tau)$, for $p = 1$, 2, 3, and 4 (Equations (3) and (4)). Results are shown in Figure 4 in terms of *B*-parallel and *B*-perpendicular structure functions (left column) and kurtosis (right). Similarly to the neutral-fluid turbulence, under the assumption of homogeneity and isotropy, the inertial range of MHD turbulence is defined as the range of scales where the third-order longitudinal structure function displays a linear dependence on the Elsässer field, $S_3 \sim \tau$. More generally, a linear dependence occurs for the longitudinal energy flux, a result known as Yaglom's four-thirds law

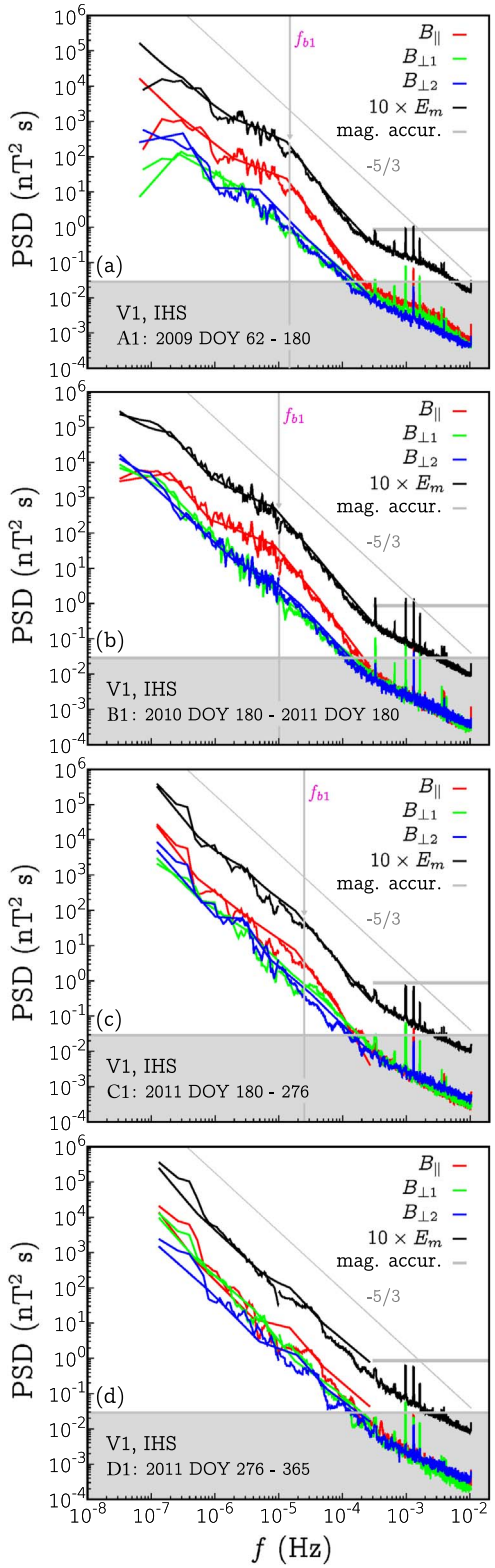

Figure 5. Power spectral density of magnetic field fluctuations at *Voyager* 1 in the IHS.

(Monin & Yaglom 1971), extended to the MHD case by Politano & Pouquet (1998). This quantity provides information on the dissipation rate of the turbulent energy and related plasma heating (Sorriso-Valvo et al. 2007; Carbone et al. 2009; Hadid et al. 2018; Sorriso-Valvo et al. 2018).

In the Kolmogorov description of (non-intermittent) isotropic and homogeneous turbulence in fluids, $S_p(\tau) \sim \tau^{p/3}$ (Kolmogorov 1941). The presence of intermittency causes the actual scaling exponents of both the velocity and the magnetic fields to deviate from the linear trend. For models and observations, we refer to She & Leveque (1994), Politano & Pouquet (1995, 1998), Bruno & Carbone (2013), and Muller & Biskamp (2000). Table 1 in Politano et al. (1998) shows a comparison of the measured exponents with different theoretical predictions.

The structure functions of the magnetic field in the IHS at *V*2 display a power-law behavior in the range of timescales that approximately corresponds to the frequency range between the spectral breaks identified in Figure 2. In the left panels of Figure 4, the red curves stand for $S_{p,\parallel}$ and the blue curves stand for $(S_{p,\perp 1} + S_{p,\perp 2})/2$ (Equation (3)). The structure functions are computed from Equation (4) and show oscillations related to data gaps. The counter $N(\tau)$ is indeed an oscillating function of τ, and it decreases linearly on average with τ (Equation (4)). When it is lower than a certain threshold (specifically, when $N(\tau) < 0.25 \max[N(\tau')]$, $\tau' \in [\tau - 48\ \mathrm{hr}, \tau + 48\ \mathrm{hr}]$), the color of the curves is switched to gray. These points were not used to compute the scaling exponents ζ_p.

As seen from the line curvature, each scaling exponent changes continuously across scales. However, the EI is easily identified, as is the effect of solar rotation. The scaling exponents and relative exponents (ζ_p^{ess}) are reported in Table 2. Fits for ζ_p have been computed in the range of τ between τ_{b1} and τ_{b2}, shown in the pictures. Relative exponents are computed by fitting S_p/S_3. The extended self-similarity principle (Benzi et al. 1993) is well verified, as S_p/S_3 show a defined power-law trend well beyond the inertial range, which allows the computation of exponents with good accuracy.

The relative exponents of parallel and perpendicular fluctuations are similar and appear to be closer to the values that are typical of plasma velocity rather than of magnetic field values (Politano & Pouquet 1995). These values are consistent with the presence of inertial-range intermittency, which is confirmed by the familiar profiles of kurtosis shown in the panels (e)–(h) of Figure 4. In fact, the intermittency increases with frequency and starts to increase at the beginning of the IC range, approximately at f_{b1}. The EI range is characterized by Gaussian values ($K \approx 3$) or is even sub-Gaussian. In the inertial-cascade range, $K(\tau)$ rises up to 10. It seems that a damping of this growth can occur at some point within the IC regime, see, e.g., the period SHS2. This is also observed at *V*1 (Figure 6, left panels). The evolution of spectral compressibility seen in Figure 3 (top) suggests the existence of a relationship between intermittency and compressibility, as has been shown by Alexandrova et al. (2008) in the kinetic regime. The decrease in compressibility and intermittency in the high-frequency range deserves further investigation. We might at present either interpret it as (i) an effect of data noise or (ii) physical reasons, as observed in Sorriso-Valvo et al. (2017) at 1 au. Again, the effect of the pickup-ion populations should be considered.

It is worth noting that the intermittency of magnetic fluctuations in the heliosheath was investigated earlier in the framework of a multi-fractal formalism (Meneveau & Sreenivasan 1987; Frisch 1995), see, e.g., Burlaga et al. (2006b), Macek et al. (2012, 2014), Burlaga & Ness (2010, 2013), and Macek & Wawrzaszek (2013). Most of the published analyses, however, are focused on the magnetic field magnitude and consider scales longer than one day. Notable exceptions are

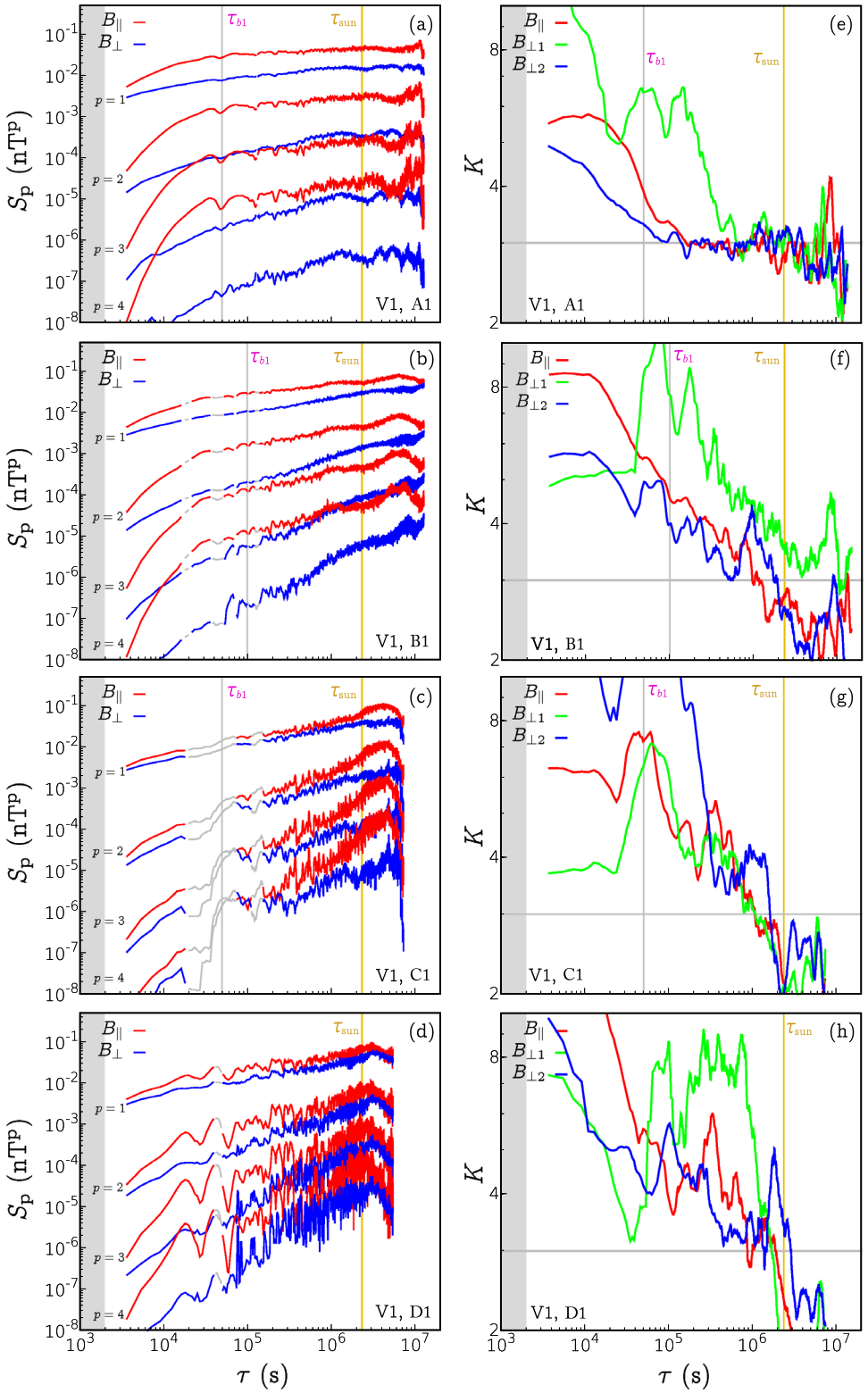

Figure 6. Structure functions (panels (a)–(d)) and kurtosis (e)–(h) at *Voyager* 1 in the IHS (see caption of Figure 4).

presented by Burlaga & Ness (2009, 2013), who consider the probability distribution functions of the increments of the magnetic field magnitude. Burlaga & Ness (2009) also used 48 s data and provided a description of different magnetic structures observed in the IHS. We point out that the low values of the multi-fractal index that are reported, e.g., by Macek et al. (2014) should not be interpreted as a non-intermittent inertial range of turbulence. In fact, their range of scales corresponds to the EI range in the present study.

3.2. *IHS Analysis of* Voyager *1 Data*

Figure 5 shows power spectra for the *V*1 intervals A1, B1, C1, and D1. Average quantities are reported in Table 3, while

Table 3
Averaged Quantities at *V*1 in the IHS

Voyager 1	A1	B1	C1	D1
r_{SC} (au)	109.5	115.7	117.9	118.8
V_0 (km s^{-1})	65	40	40	40
B_0 (nT)	0.083	0.132	0.195	0.124
B (nT)	0.086	0.140	0.203	0.148
f_{cp} (mHz)	1.32	2.14	3.10	0.81

Note. Because the PLS subsystem is not operative, the velocity is derived from the LECP and CRS subsystems. Here, we report data from Figure 1 in Krimigis et al. (2011) and Figure 1 in Richardson & the Voyager Team (2016).

the fluctuation statistics, spectral breaks and slopes, and structure-function exponents are shown in Table 4. Spectral compressibility is shown in Figure 3 (bottom panel), and high-order statistics are shown in Figure 6.

At *V*1, the intensity of the magnetic fluctuations is in general lower than at *V*2. The contribution to the fluctuating energy is largely due to the $\delta B_{\parallel}$ components, which results in much higher values of compressibility ($C_1 \approx 0.6$), especially during 2009-2011.5.

Because Taylor's hypothesis does not hold at *V*1, we did not convert spacecraft frequencies to wavenumbers, and all figures show the spacecraft-frame frequency axis alone. In the early periods A1 and B1, the spectra show a marked difference between *B*-parallel and *B*-perpendicular fluctuations, $\delta B_{\parallel}$ being more energetic than $\delta B_{\perp}$ by a factor as high as five in the central decades of the spectrum. Details on variance anisotropy are given in Figure 11 in Appendix B, where it is shown that $P[B_{\perp}]/P[B_{\parallel}] < 1$ in the proximity of the spectral break observed at $f_{b1} \approx 10^{-5}$ Hz. This corresponds to the presence of compressive modes. In fact, $P[|\boldsymbol{B}|]/E_m$ reaches maximum at f_{b1} (see Figure 3, bottom, and the black curves in the left panels of Figure 11). At lower frequencies, the spectral index of the total energy is $\alpha_1 \approx -1.2$ (black curves in Figure 5), while beyond the break, a fast steepening occurs, with the slopes as high as $\alpha_2 \approx -2.3$. Again, the shape of the spectral trace is mainly due to $\delta B_{\parallel}$, which displays a rather fast cascade in the range $10^{-5} \lesssim f \lesssim 10^{-4}$ Hz ($\alpha_{2,\parallel} \approx -2.5$). The two perpendicular components behave similarly to each other, and on average, they experience a Kolmogorov-like spectral decay in the whole range of frequencies, with an index between -1.35 and -1.8. In the later periods C1 and D1, which are closer to the HP boundary, the spectral break becomes weaker even for $\delta B_{\parallel}$, so that the discrepancy between the components is significantly reduced (see the bottom panels in Figure 5 and the left panels of Figure 11). In fact, the level of compressibility decreases to 0.4 during D1 at all frequencies.

At frequencies higher than about 10^{-4} Hz, the spectra flatten, likely due to the lower limit of data accuracy. The curved shape at $10^{-3} < f < 10^{-2}$ Hz during A1 suggests, however, that physical phenomena such as wave-particle interaction or PUI-driven turbulence may still be relevant in the signal.

The profiles of parallel structure functions (red curves in Figure 6, left column) show a well-defined change in the power law on the timescales corresponding to the observed spectral break. The exponents ζ_p reported in Table 4 have been fitted in the range $\tau \in [10^4 \text{ s}, \tau_{b1}]$ for A1 and B1, and $\tau \in [10^4, 2 \times 10^5]$ s for C1 and D1. Thus, we show the exponents of S_p for the $\alpha \approx -2$ part of the power spectra. Relative exponents instead hold for the whole range of frequencies. Moreover, at *Voyager* 1, the fluctuations are intermittent (right panels of Figure 6). In addition to previous large-scale analyses (e.g., Burlaga et al. 2006a; Macek et al. 2014), we show that the kurtosis profiles of magnetic increments increase with increasing frequency for all intervals. It should be noted, however, that the growth starts within the range $\tau \in [10^5, 10^6]$ s. This was expected for the $B_{\perp}$ components, but not so for $B_{\parallel}$: is seems that the intermittency of the compressible component starts prior to the energy spectral break, at about $f \approx 10^{-6}$ Hz, except for the interval A1.

4. LISM Magnetic Turbulence

Figure 7 shows the power spectra of the ISMF in the four *V*1 intervals L1–L4. Anisotropy is shown in Figure 12 in Appendix B. As shown in the summary Table 5, the intensity of magnetic fluctuations with respect to the background field ($B_{0\,\mathrm{LISM}} \approx 0.5$ nT) is nearly one order of magnitude lower than in the IHS. The fluctuating magnetic energy increases significantly in the later periods L3 and L4, and L1 is the quietest interval. There is little variation in the rms of parallel fluctuations among the intervals, even though it is higher during the central periods L2 and L3. In fact, the central periods are the most compressible ($C \approx 0.5$). We observe a progressive increase in transverse fluctuations in the $\perp_2$ (radial) direction. In fact, during L4, magnetic fluctuations are primarily transverse, especially at the largest scales, as highlighted in Figure 8 (pink curve) and in Figure 12(h). This fact was first pointed out by Burlaga et al. (2018).

The power spectra shown in the left panels of Figure 7 contain five frequency decades, a range unexplored so far. The figure shows the noise level corresponding to white noise with 0.04 nT amplitude (gray bands), i.e., $P_{\mathrm{noise}} \approx 0.05$ nT^2 s. Burlaga et al. (2018) indicate that noise may affect the data at $f \gtrsim 4 \times 10^{-5}$ Hz, which is consistent with the spectral flattening we observe. It is interesting to note, however, that the level of anisotropy in this range remains high, at values around 0.45, and that different profiles are shown across intervals (Figure 8), which might be indicative of less noise than estimated.

However, one can observe a spectral flattening (or a small bump) that occurs for all periods in the range $10^{-6} < f < 10^{-5}$ Hz. Moreover, the ion cyclotron frequency is lower than in the IHS, $f_{\mathrm{ci,LISM}} \approx 10^{-4}$ Hz. At lower frequencies, the energy decays as a power law with spectral index close to the Kolmogorov $-5/3$ value. The values reported in Table 5 have been computed in the range $5 \times 10^{-8} < f < 3 \times 10^{-6}$ Hz. As usual, errors indicate the discrepancy between the three spectral estimation techniques, and this discrepancy is higher than in the IHS because only the first decade is considered. It should be noted that in the interval L2, a spectral flattening occurs at the lower frequencies ($f < 3 \times 10^{-7}$ Hz). This may indicate that the turbulence is young and locally generated or, alternatively, affected by local structures as shocks. During L4, magnetic fluctuations seem to change nature because transverse fluctuations (both along $\perp_1$ and $\perp_2$) become dominant and a clear power-law decay of energy is observed, with a spectral index about -1.9 that is in part due to some rapid shears in the signal. The parallel cascade is much slower, $\alpha \approx -1.4$.

The LISM turbulence is expected to show the features of intermittency, which has not been considered in the literature so far. Our results are shown in Figures 7(e)–(h), which show the scale-dependent kurtosis of magnetic increments, as was done for the IHS data in the previous section. We see that there is no intermittency at timescales $\tau \gtrsim 10^6$ s for all intervals

Table 4
Magnetic Field Fluctuation Properties at *V1* in the IHS

	A1	B1	C1	D1
E_m (nT^2)	1.67×10^{-3}	5.03×10^{-3}	4.50×10^{-3}	4.05×10^{-3}
C_1	0.61	0.55	0.62	0.42
C_2	0.95	0.76	0.74	0.62
$I_\parallel$	0.34	0.40	0.24	0.28
$I_{\perp 1}$	0.11	0.17	0.10	0.27
$I_{\perp 2}$	0.13	0.22	0.12	0.13
I	0.42	0.54	0.31	0.46
δB_{mv}	0.037	0.061	0.069	0.055
θ_{mv}	166°	147°	141°	42°
f_{b1} (Hz)	2×10^{-5}	10^{-5}	2×10^{-5}	…
α_1	-1.17 ± 0.09	-1.31 ± 0.15	-1.60 ± 0.18	…
α_2	-2.25 ± 0.12	-2.31 ± 0.04	-2.23 ± 0.09	-1.72 ± 0.05
$f_{b1\parallel}$ (Hz)	2×10^{-5}	10^{-5}	2×10^{-5}	…
$\alpha_{1\parallel}$	-1.18 ± 0.06	-1.21 ± 0.07	-1.45 ± 0.10	-1.95 ± 0.10
$\alpha_{2\parallel}$	-2.65 ± 0.10	-2.50 ± 0.03	-2.52 ± 0.10	-1.80 ± 0.05
$f_{b1\perp}$ (Hz)	4×10^{-6}	…	…	…
$\alpha_{1\perp}$	-1.35 ± 0.04	-1.52 ± 0.05	-1.57 ± 0.09	-1.76 ± 0.10
$\alpha_{2\perp}$	-1.59 ± 0.13	-1.77 ± 0.06	-1.70 ± 0.1	-1.80 ± 0.05
$\zeta_{1,\parallel}$($\zeta^{ess}_{1,\parallel}$)	0.48 (**0.38**)	0.62 (**0.36**)	0.44 (**0.39**)	0.36 (**0.33**)
$\zeta_{2,\parallel}$ ($\zeta^{ess}_{2,\parallel}$)	0.93 (**0.71**)	1.19 (**0.70**)	0.90 (**0.72**)	0.62 (**0.65**)
$\zeta_{3,\parallel}$ ($\zeta^{ess}_{3,\parallel}$)	1.31 (1)	1.63 (1)	1.34 (1)	0.81 (1)
$\zeta_{4,\parallel}$ ($\zeta^{ess}_{4,\parallel}$)	1.64 (**1.24**)	1.99 (**1.24**)	1.72 (**1.27**)	0.98 (**1.23**)
$\zeta_{1,\perp}$ ($\zeta^{ess}_{1,\perp}$)	0.34 (**0.36**)	0.41 (**0.36**)	0.43 (**0.32**)	0.36 (**0.38**)
$\zeta_{2,\perp}$ ($\zeta^{ess}_{2,\perp}$)	0.67 (**0.70**)	0.81 (**0.69**)	1.02 (**0.66**)	0.74 (**0.70**)
$\zeta_{3,\perp}$ ($\zeta^{ess}_{3,\perp}$)	0.97 (1)	1.17 (1)	0.87 (1)	1.14 (1)
$\zeta_{4,\perp}$ ($\zeta^{ess}_{4,\perp}$)	1.23 (**1.24**)	1.48 (**1.25**)	2.30 (**1.35**)	1.56 (**1.28**)

because the kurtosis is smaller than three. At smaller scales, intermittency is observed for the $\perp_1$ component alone in the first three periods. During L4, instead, a significant increase in kurtosis is observed for both $\perp_1$ and $\perp_2$ in the range $10^5 \lesssim \tau \lesssim 3 \times 10^6$ s, where the energy cascade is fast. It should be noted that in the noisy range ($\tau \lesssim 10^4$ s), the statistic returns to Gaussian. Moreover, during L1 and L4, the reduction of K starts at larger scales, at about $\tau \approx 3 \times 10^5$ s. This corresponds to the flattening observed in the power spectrum. Although it is possible that this reduction is an artifact due to data uncertainty, it does not occur systematically. At the current state of our analysis we therefore do not exclude physical reasons. Increments of parallel fluctuations never show strong intermittency (differently to what was observed in the IHS).

The structure-function exponents reported in Table 5 have been computed in the range $\tau = [5 \times 10^5, 5 \times 10^6]$ s. The absence of intermittency at larger scales may be a result of the passage of shocks—which could have caused the pristine interstellar fluctuations to become more Gaussian—or a signature of locally produced turbulence. The possibility that MHD waves could be transmitted from the IHS to the LISM has also been described (Zank et al. 2017).

5. Summary and Final Remarks

This work provides a broadband spectral and high-order statistical analyses of magnetic field fluctuations in the IHS and LISM that give new insights into the properties of turbulence and its evolution. Our aim was to investigate the existence of different regimes of turbulent fluctuations, characterize them, and describe their evolution in time and space.

We considered 12 data sets at different times and latitudes obtained after 2009, at between 88 and 135 au. The analysis of high-resolution (48 s) in situ measurements from both the *Voyager* 1 and *2* spacecraft with the proposed advanced spectral estimation techniques made it possible to investigate the evolution of fluctuations across more than five frequency decades ($10^{-8} < f < 10^{-2}$ Hz), a range of scales that has not been explored in the literature so far. We focused our attention on the energy cascade, the compressible nature, anisotropy, and intermittency of magnetic fluctuations.

In the IHS at *V2*, we identified the EI and inertial-cascade regimes. Instead, the signatures of the kinetic regime were expected to be observed in the last decade of the frequency spectrum ($10^{-3} < f < 10^{-2}$ Hz), but at present, the unknown exact level of noise in data does not allow us to discuss this regime. However, we believe that physical phenomena may still be detected in this range, so that it deserves further study.

The EI range is featured by a $1/f$ power-law decay of magnetic energy, non-intermittent statistics of magnetic increments, and low compressibility. Its frequency extent depends on the observational interval considered, and it seems to be wider in the unipolar periods. The first relevant scale highlighted in this study corresponds the EI/IC spectral break,

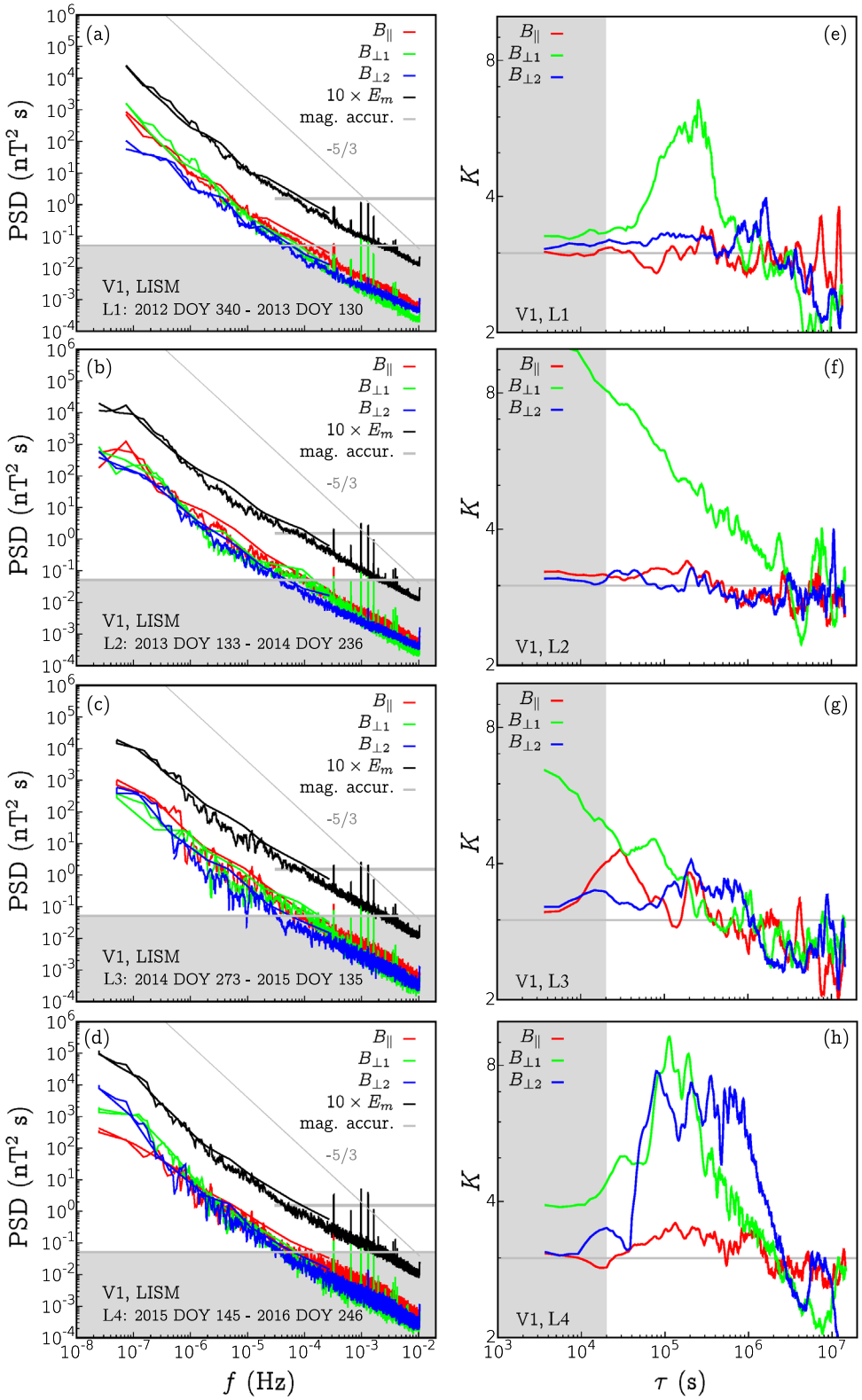

Figure 7. Local interstellar medium. Left panels (a)–(d): Power spectral density of magnetic field fluctuations. Right panels (e)–(h): Kurtosis of magnetic field increments for each field component.

and could be related neither to the nominal spacing of sectors (≈2 au) alone nor to the age of fluctuations generated or affected by the TS. In the unipolar periods, for instance, the spectral break occurs at $f \approx 10^{-5}$ Hz, corresponding to a spatial scale of about 0.15 au along the wind direction. The originally more Alfvénic nature of unipolar regions may explain the observed difference between SHS and UHS periods.

The IC regime is characterized by (i) a steepening of power spectra toward values of spectral index close to the Kolmogorov value of −1.67, (ii) a rapid growth of the kurtosis of

Table 5
Magnetic Field Fluctuation Properties in the LISM

	L1	L2	L3	L4
E_m (nT^2)	2.84×10^{-4}	2.38×10^{-4}	3.72×10^{-4}	6.86×10^{-4}
C_1	0.30	0.40	0.48	0.12
C_2	0.41	0.54	0.65	0.12
$I_\parallel$	0.014	0.018	0.023	0.015
$I_{\perp 1}$	0.019	0.016	0.014	0.030
$I_{\perp 2}$	0.009	0.012	0.014	0.038
I	0.029	0.030	0.035	0.057
δB_{mv}	0.013	0.011	0.015	0.019
θ_{mv}	65°	23°	173°	98°
α	-1.57 ± 0.05	-1.65 ± 0.10	-1.55 ± 0.10	-1.77 ± 0.10
$\alpha_\parallel$	-1.59 ± 0.05	-1.60 ± 0.10	-1.57 ± 0.10	-1.40 ± 0.06
$\alpha_\perp$	-1.54 ± 0.02	-1.60 ± 0.05	-1.54 ± 0.10	-1.90 ± 0.05
$\zeta_{1,\parallel}$ ($\zeta^{ess}_{1,\parallel}$)	0.18 (**0.33**)	0.15 (**0.34**)	0.14 (**0.38**)	0.15 (**0.35**)
$\zeta_{2,\parallel}$ ($\zeta^{ess}_{2,\parallel}$)	0.36 (**0.67**)	0.28 (**0.68**)	0.27 (**0.71**)	0.29 (**0.68**)
$\zeta_{3,\parallel}$ ($\zeta^{ess}_{3,\parallel}$)	0.55 (1)	0.40 (1)	0.39 (1)	0.43 (1)
$\zeta_{4,\parallel}$ ($\zeta^{ess}_{4,\parallel}$)	0.73 (**1.32**)	0.51 (**1.31**)	0.49 (**1.25**)	0.56 (**1.30**)
$\zeta_{1,\perp}$ ($\zeta^{ess}_{1,\perp}$)	0.35 (**0.36**)	0.25 (**0.38**)	0.21 (**0.40**)	0.40 (**0.43**)
$\zeta_{2,\perp}$ ($\zeta^{ess}_{2,\perp}$)	0.67 (**0.71**)	0.48 (**0.71**)	0.37 (**0.72**)	0.72 (**0.76**)
$\zeta_{3,\perp}$ ($\zeta^{ess}_{3,\perp}$)	0.96 (1)	0.69 (1)	0.5 (1)	0.96 (1)
$\zeta_{4,\perp}$ ($\zeta^{ess}_{4,\perp}$)	1.21 (**1.23**)	0.88 (**1.24**)	0.59 (**1.24**)	1.12 (**1.17**)

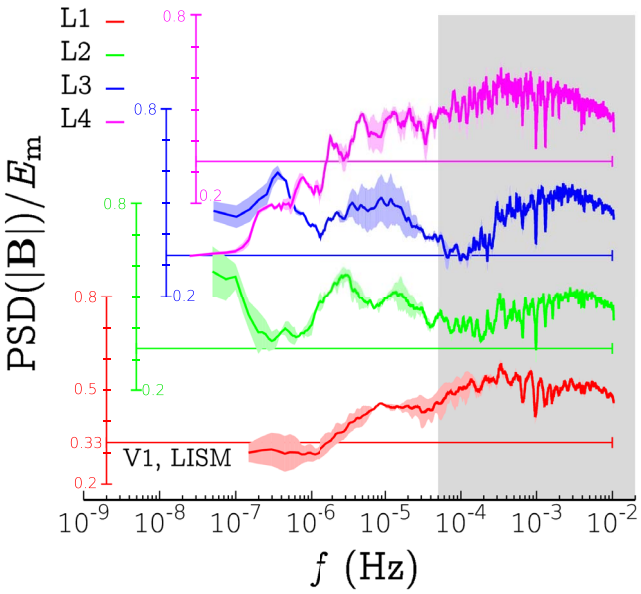

Figure 8. Spectral compressibility in the LISM. Average values computed through Equation (1) are shown in Table 5.

magnetic field increments, and (iii) a clearly defined power-law decay of the third-order structure function S_3, with typical exponents of MHD turbulence. It can be concluded that unipolar periods showed a faster energy decay than sectored periods. The second typical scale in the $V2$ analysis was observed at $f \approx 10^{-4}$ Hz ($\ell \approx 5 \times 10^{-3}$ au). Here, a spectral knee occurs mainly for $\delta B_\parallel$, and maximum anisotropy and compressibility is observed.

Fluctuations in the broad unipolar regions traveled by $V1$ before 2011.5 show a marked dominance of $\delta B_\parallel$. Parallel energy experiences a spectral break that separates the large-scale regime with slow $1/f$ decay from the fast regime with $\alpha \approx -2.5$. Interpretation of $V1$ spectra is challenging due to the lack of accurate plasma velocity data and slow-wind conditions, which do not allow us to compute the wavenumbers. It is possible that the parallel-wavenumber components due to Alfvénic or fast magnetosonic fluctuations dominate the spacecraft-frame frequency, but at present, we cannot verify this hypothesis. We showed that $V1$ fluctuations are intermittent with a power-law increase in kurtosis anticipating a spectral break. A similar trend is also observed for the spectral compressibility, which reaches maximum at the break frequency.

Finally, we have analyzed four LISM intervals. Even in this case, we used 48 s data to extend the range of frequencies considered in past literature studies and to improve the accuracy of spectral estimates. We note that the level of compressible fluctuations is not higher than 0.6, and we confirm the recently observed change of nature of turbulence during 2015/2016. This transition mainly consists of an increase in perpendicular energy (especially in the $\perp_2$ component). Moreover, in all intervals we observed a spectral flattening resembling a small bump, for $10^{-6} \lesssim f \lesssim 10^{-5}$ Hz. This bump also corresponds to an increase in compressibility. Its nature should be further investigated. Intermittency is mainly observed in transverse fluctuations. This rapid increase begins at a spacecraft frequency of 3×10^{-7} Hz. It is then plausible that the observed LISM turbulence is locally modified by the periodic passage of shocks.

We expect our results to provide additional constraints on numerical and theoretical models of the outer heliosphere and to hopefully shed light onto transport properties of energetic particles in these regions of space.

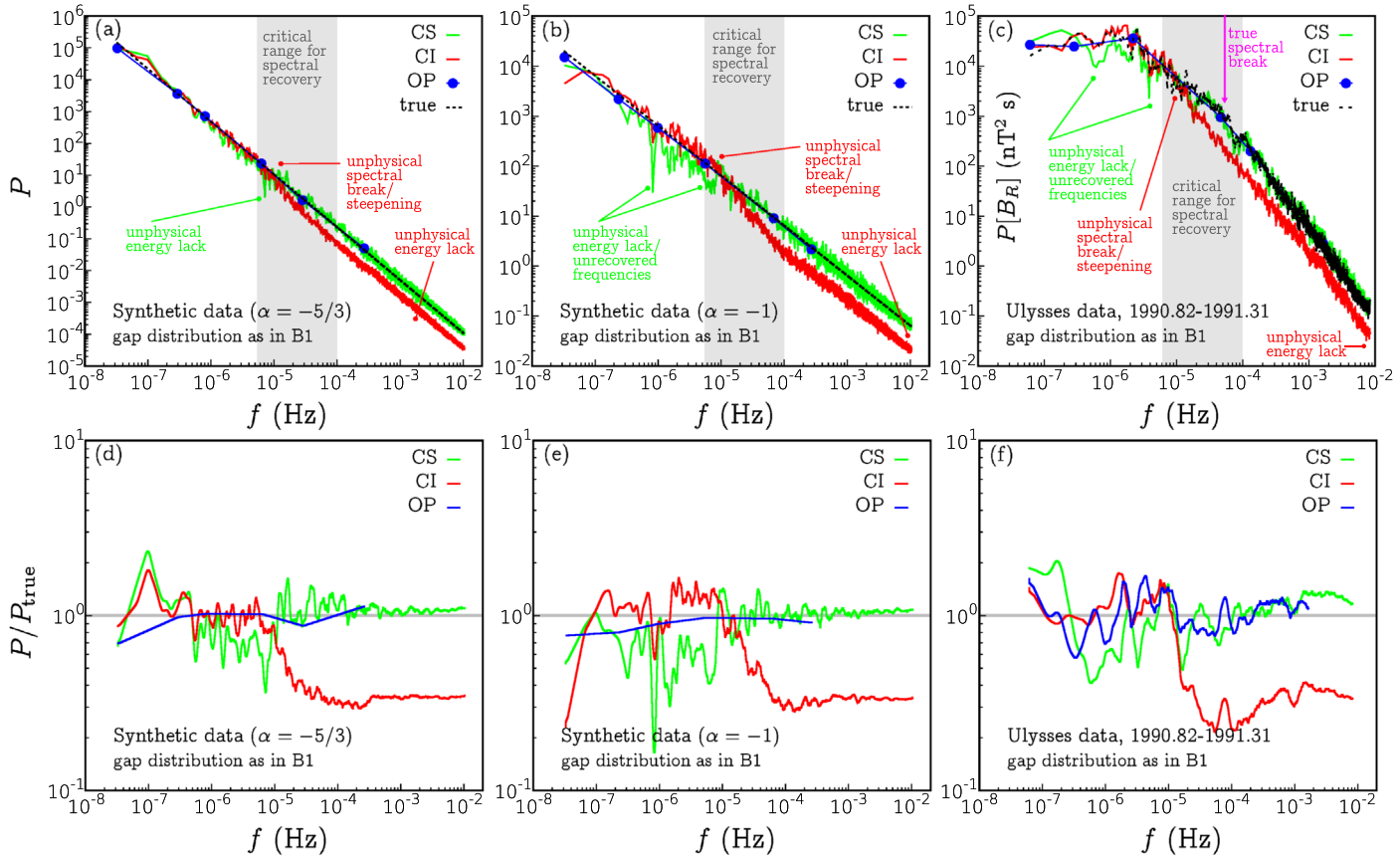

Figure 9. Testing of spectral estimation techniques on synthetic turbulence data with constant spectral index, $\alpha = -5/3$ in panels (a) and (d); synthetic turbulence data with $\alpha = -1$ in panels (b) and (e); and *Ulysses* data (1990.82-1991.31, gap-free) in panels (c) and (f). The top panels show the PSD, and the bottom panels show the ratio between the estimated and the true spectrum. In these tests, data points have been artificially removed with the same gap distribution as in period B1 (68% of missing points; longest gap: 132 hr; longest gap-free subset length: 16.5 hr; and average gap-free subset length: 3.25 hr).

We thank the anonymous referee for helpful comments and suggestions. The authors acknowledge support from the MISTI-Seeds MITOR project "Spectral analysis of the solar wind beyond the termination shock—interstellar medium/heliosphere interactions" 2015–2016. F.F. was also supported by the postdoctoral grant "FOIFLUT" 37/17/F/AR-B. N.P. was supported, in part, by NASA grants NNX14AJ53G, NNX16AG83G, and 80NSSC18K1649NS, and by the NSF PRAC award OAC-1811176. J.D.R. was supported under NASA contract 959203 from JPL to MIT. Computational resources for spectral and statistical analysis were provided by HPC@POLITO (http://www.hpc.polito.it).

Appendix A
Methods for Spectral Analysis

Computing power spectra over a broad range of frequencies in the outer heliosphere is challenging because of the sparsity of the 48 s data (70% of the magnetic field are missing). Fraternale et al. (2016), Gallana et al. (2016), Iovieno et al. (2016), and Fraternale (2017) have demonstrated that a careful application of different independent techniques enables recovering the spectrum with proper accuracy (e.g., with an accuracy of 10% or lower in the spectral index). The technique description and numerical codes have been provided in the above references. Here, we briefly recall them with a focus on their specific application to *Voyager* data in the IHS, together with three examples of tests conducted on contiguous data sets that were artificially gapped (synthetic turbulence and *Ulysses* data, see Figure 9).

1. *Correlation method with linear data interpolation* (CI): The PSD is obtained as the Fourier transform of the two-point auto-covariance function computed from linearly interpolated data. It recovers the spectrum well in the low-frequency range, i.e., at frequencies lower than the typical frequency of large data gaps ($f_{\rm gap} \approx 2 \times 10^{-5}$ Hz). Due to the low-pass effect of the linear interpolation, spectral leakage is observed at higher frequencies and spectral exponents are typically overestimated (70% energy loss, see the bottom panels in Figure 9, red curves).
2. *Compressed sensing spectral estimation* (CS): A recent paradigm we adopted from the signal processing and telecommunication area (Candes et al. 2006a, 2006b; Donoho 2006). This method does not interpolate data. It allows exactly recovering sparse signals (signals with only few nonzero frequencies) even if fewer data points than those required by Shannon's principle are available. Testing CS on turbulent, gapped data sets, we found that it recovers the spectrum well, especially the high-frequency range ($f \gtrsim f_{\rm gap}$). Depending on the interval considered, it may lack accuracy in the neighborhood of $f_{\rm gap}$. This typically shows up as a lack of energy around $f \in [3 \times 10^{-6}, 10^{-5}]$ Hz (green curves in Figure 9). Moreover, a small peak around

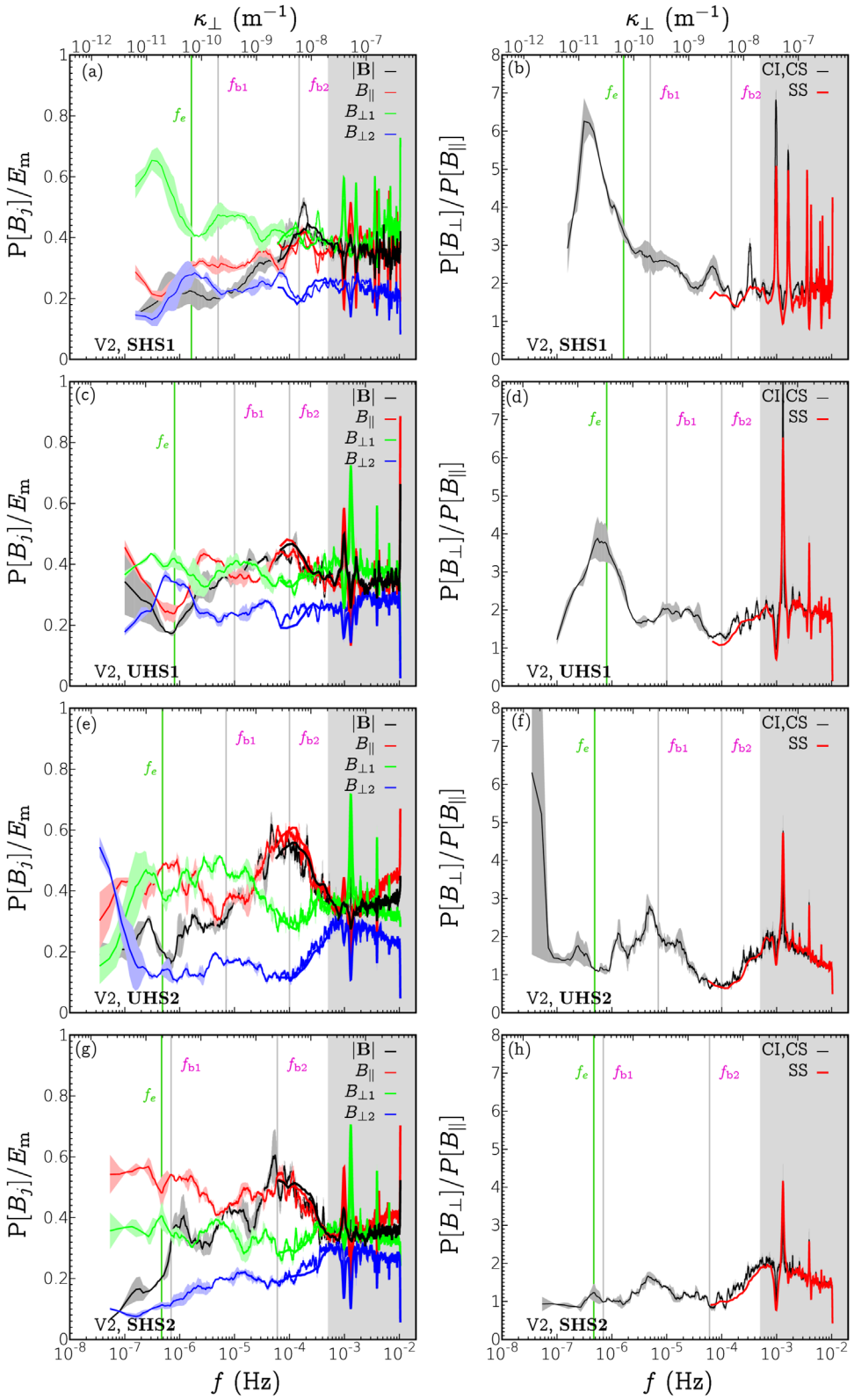

Figure 10. Spectral variance anisotropy and compressibility in the IHS at *Voyager* 2. Top to bottom: Intervals SHS1, UHS1, UHS2, and SHS2. Left panels: Anisotropy computed as $P[B_j]/E_m$, where $B_j = \{B_\parallel, B_{\perp 1}, B_{\perp 2}, |\boldsymbol{B}|\}$, and E_m is the trace. The black curve represents the spectral compressibility proxy, based on the magnetic field magnitude. The thick continuous lines stand for the SS method (gap-free subsets), the thin curves show the average result of methods CI and CS, together with error bands. Right panels: Ratio between B-perpendicular and B-parallel energy. Here, black lines show the average result of methods CI and CS (with error bands), and red lines show the result from contiguous subsets (SS). The peaks in the last decade are due to instrumental interference.

$f_{\rm gap}$ is sometimes observed (see the case of SHS2, Figure 2(d)). CS has also recently been exploited for the analysis of the spectrum of magnetospheric intervals out of a Kelvin–Helmholtz-instability event observed by the *Magnetospheric Multiscale mission* in the Earth magnetosphere (Sorriso-Valvo et al. 2019).

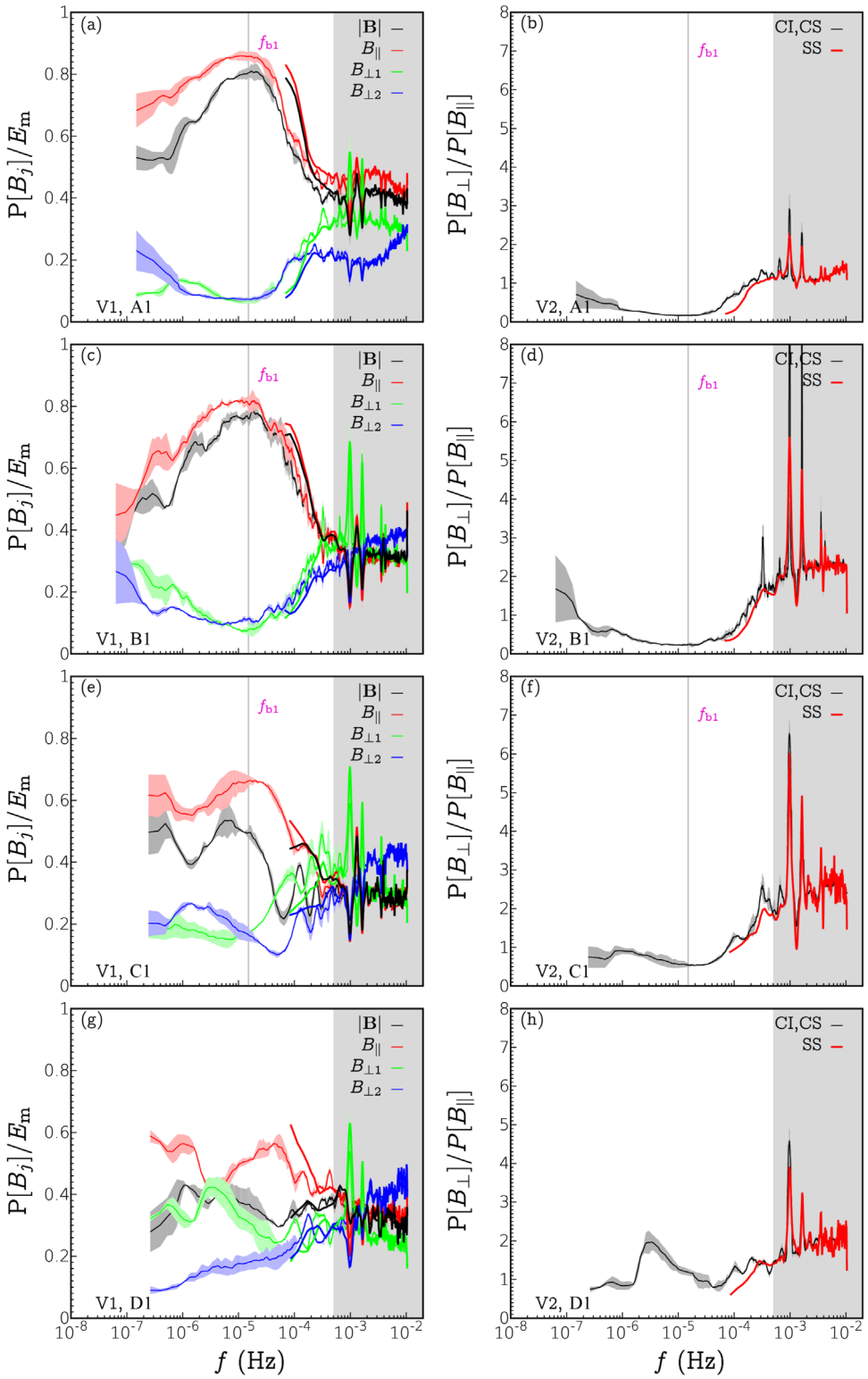

Figure 11. Spectral variance anisotropy and compressibility in the IHS at *Voyager* 1. Top to bottom: Intervals A1, B1, C1, and D1. The panel description is the same as in the caption of Figure 10.

3. *Optimization method* (OP): This is a simple algorithm that aims at minimizing errors in the CI analysis. This method is based on a genetic algorithm (Charbonneau 1995, our code is based on the open-source code PIKAIA) that returns the piecewise-linear model spectrum, $P_{OP}(f)$ as a result. Starting from an initial model spectrum, a synthetic signal is obtained by inverse Fourier transform. From this synthetic set, some data are removed according to the gap distribution in the *Voyager* data set. The power spectrum of this gapped synthetic set is successively computed by using the CI technique ($P_{sy,CI}$). The result is then compared to the CI spectrum of the *Voyager* data set ($P_{voy,CI}$). The difference

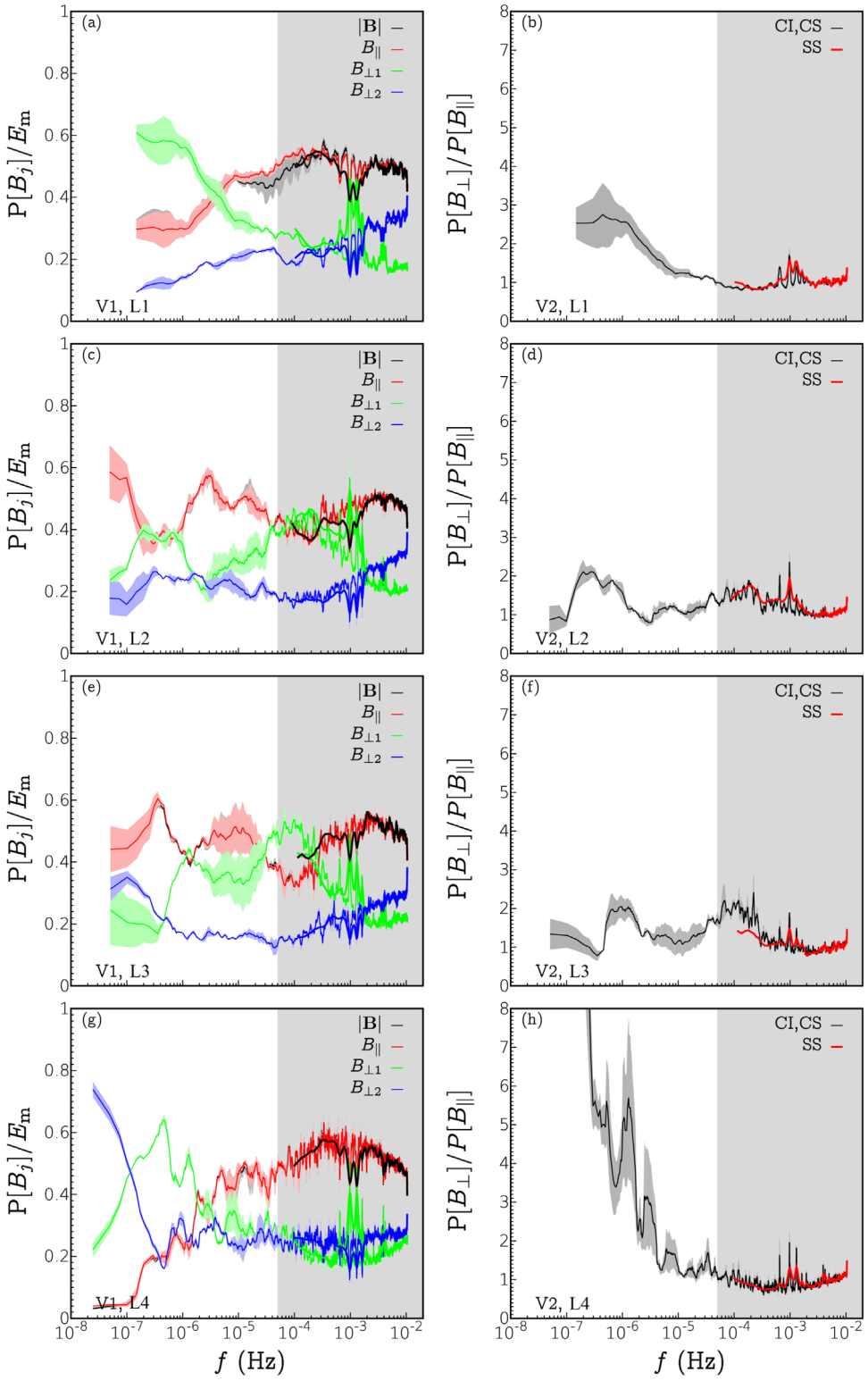

Figure 12. Spectral variance anisotropy and compressibility in the LISM at *Voyager* 1. Top to bottom: Intervals L1, L2, L3, and L4. The panel description is the same as in the caption of Figure 10.

between the two spectra ($F = \sum_i |P_{\mathrm{sy,CI}}(f_i) - P_{\mathrm{voy,CI}}(f_i)|$) is minimized by the optimization algorithm, which at each generation modifies the control points in the model spectrum that is an approximation of the true spectrum of the *Voyager* signal (Fraternale 2017, Chapt. 4). This method helps to estimate the error of the linear interpolation. Heuristically, OP proved to work well for statistically homogeneous data sets representing physical phenomena with a continuous spectrum distributed over a broad range of scales. It cannot represent peaks in the spectrum, but if there were any, they were well identified by the other methods above (Figure 9, blue curves).

4. *Gap-free subsets* (SS): To check results in the high-frequency range, we compute the averaged spectrum of contiguous subsets. Given the gap distribution of IHS and LISM *Voyager* data, this allows us to see the frequency range $10^{-4} \lesssim f \lesssim 10^{-2}$ Hz. In fact, for all intervals considered in this study, the average subset length is 3.7 ± 0.6 hr in the IHS and 2.49 ± 0.07 in the LISM; the maximum length is 14.4 ± 3.3 hr in the IHS and 10.3 ± 2.3 in the LISM. On average, ensambles include 520 subsets (Figures 10–12).

The power spectra displayed in Figures 2, 5, and 7 are built using the average result of CI and CS for $f < 10^{-5}$ Hz, and for $f > 10^{-5}$ Hz CS alone. The results of the OP method are also shown in all PSD pictures by a continuous smooth curve. In general, a very good agreement is observed. Note also that the CI and CS spectra are smoothed by means of a moving average with a constant-width window in the logarithmic space (i.e., the averaging points increase linearly with the frequency). This smoothing has no effect on the power level and on the spectral index.

Figure 9 shows the application of methods CI (red curves), CS (green curves), and OP (blue curves) to three data sets, where data have been artificially removed according to the same gap distribution of period B1. The first data set is a synthetic turbulence set (obtained by inverse transform of a given power spectrum—black line—using random phases of the Fourier coefficients) with a constant index $\alpha = -5/3$ (Figure 9(a)). In the second case $\alpha = -1$, which represents a harder test case (panel b). In the third case, we used gap-free *Ulysses* data in the period 1990.82-1991.31. Panels (d)–(f) show the (smoothed) ratio between the estimated and the true spectrum $P/P_{\rm true}$.

It should be noted that—due to the gap distribution of *Voyager* magnetic field time series in the IHS and LISM—the frequency range where spectral estimation is more critical is around $10^{-5} < f < 10^{-4}$ Hz. The lower bound corresponds to $f_{\rm gap} \approx 2 \times 10^{-2}$ Hz, the higher is linked to the length of contiguous subsets.

Appendix B
Variance Anisotropy

Figures 10–12 show the frequency-space anisotropy for all IHS and LISM intervals presented in this study. The left panels show the fractional energy of each magnetic field component with respect to the trace, that is, $P[B_j]/E_m$. The $|\boldsymbol{B}|$ case, black curves, is the spectral compressibility proxy already shown in Figures 3 and 8. From the left panels, one can see that the $\delta B_{\parallel}$ curve (red) follows the $|\boldsymbol{B}|$ curve (black) in most cases, especially for $f > 10^{-5}$ Hz (a worse agreement is observed for C1 and D1 periods, which are shorter than others). Some discrepancy between the two curves is observed in sectored regions in the low-frequency regime: this is due to tangential discontinuities in correspondence of sector boundary crossings (here, $B_{\parallel}$ changes sign). Such reversals are seen in the spectrum as large-amplitude $\delta B_{\parallel}$ fluctuations, but are not related to compressions. In fact, they are not accounted for by the $P[|\boldsymbol{B}|]/E_m$ indicator. The peak of compressibility and anisotropy occurs at $f_{\rm b2}$ for *V*2 and at $f_{\rm b1}$ for *V*1. Note also that a significant level of anisotropy is retained in the gray region, where data may be affected by noise, especially in the LISM (Figure 12).

ORCID iDs

Federico Fraternale https://orcid.org/0000-0002-4700-2762
Nikolai V. Pogorelov https://orcid.org/0000-0002-6409-2392
John D. Richardson https://orcid.org/0000-0003-4041-7540
Daniela Tordella https://orcid.org/0000-0002-4639-0572

References

Aggarwal, P., Taylor, D. K., Smith, C. W., et al. 2016, ApJ, 822, 94
Alexandrova, O., Carbone, V., Veltri, P., & Sorriso-Valvo, L. 2008, ApJ, 674, 1153
Alexandrova, O., Lacombe, C., Mangeney, A., Grappin, R., & Maksimovic, M. 2012, ApJ, 760, 121
Behannon, K. W., Acuna, M. H., Burlaga, L. F., et al. 1977, SSRv, 21, 235
Benzi, R., Ciliberto, S., Tripiccione, R., et al. 1993, PhRvE, 48, R29
Berdichevsky, D. B. 2009, Voyager Mission, Detailed processing of weak magnetic fields; II - Update on the cleaning of Voyager magnetic field density B with MAGCALs (Washington, DC: NASA)
Bieber, J. W., Wanner, W., & Matthaeus, W. H. 1996, JGRA, 101, 2511
Borovikov, S. N., & Pogorelov, N. V. 2014, ApJL, 783, L16
Borovikov, S. N., Pogorelov, N. V., Burlaga, L. F., & Richardson, J. D. 2011, ApJL, 728, L21
Bruno, R., & Carbone, V. 2013, LRSP, 10, 2
Bruno, R., Carbone, V., Vörös, Z., et al. 2009, EM&P, 104, 101
Bruno, R., Telloni, D., & Sorriso-Valvo, L. 2018, Geophys. Research Abstracts (Vienna: European Geosciences Union General Assembly), 2018
Burlaga, L. F. 1994, JGR, 99, 19341
Burlaga, L. F., Florinski, V., & Ness, N. F. 2015, ApJL, 804, L31
Burlaga, L. F., Florinski, V., & Ness, N. F. 2018, ApJ, 854, 20
Burlaga, L. F., & Ness, N. F. 2009, ApJ, 703, 311
Burlaga, L. F., & Ness, N. F. 2010, ApJ, 725, 1306
Burlaga, L. F., & Ness, N. F. 2012, ApJ, 744, 51
Burlaga, L. F., & Ness, N. F. 2013, ApJ, 765, 35
Burlaga, L. F., & Ness, N. F. 2014a, ApJL, 795, L19
Burlaga, L. F., & Ness, N. F. 2014b, ApJ, 784, 146
Burlaga, L. F., & Ness, N. F. 2016, ApJ, 829, 134
Burlaga, L. F., Ness, N. F., & Acuna, M. H. 2006a, ApJ, 642, 584
Burlaga, L. F., Ness, N. F., & Acuna, M. H. 2006b, JGRA, 111, A09112
Burlaga, L. F., Ness, N. F., & Acuna, M. H. 2007, ApJ, 668, 1246
Burlaga, L. F., Ness, N. F., Acuna, M. H., Wang, Y. M., & Sheeley, N. R., Jr. 2009, JGRA, 114, A06106
Burlaga, L. F., Ness, N. F., Gurnett, D. A., & Kurth, W. S. 2013a, ApJL, 778, L3
Burlaga, L. F., Ness, N. F., & Richardson, J. D. 2017, ApJ, 841, 47
Burlaga, L. F., Ness, N. F., & Stone, E. C. 2013b, Sci, 341, 147
Burlaga, L. F., Wang, C., & Ness, N. F. 2003a, GeoRL, 30, 1543
Burlaga, L. F., Wang, C., Richardson, J. D., & Ness, N. F. 2003b, ApJ, 590, 554
Burlaga, L. F., Wang, C., Richardson, J. D., & Ness, N. F. 2003c, JGRA, 108, 1305
Bzowski, M., Mobius, E., Tarnopolski, S., Izmodenov, V., & Gloeckler, G. 2009, SSRv, 143, 177
Candes, E. J., Romberg, J. K., & Tao, T. 2006a, ITIT, 52, 489
Candes, E. J., Romberg, J. K., & Tao, T. 2006b, CPAM, 59, 1207
Cannon, B. E., Smith, C. W., Isenberg, P. A., et al. 2014a, ApJ, 787, 133
Cannon, B. E., Smith, C. W., Isenberg, P. A., et al. 2014b, ApJ, 784, 150
Carbone, V., Marino, R., Sorriso-Valvo, L., Noullez, A., & Bruno, R. 2009, PhRvL, 103, 061102
Charbonneau, P. 1995, ApJS, 101, 309
Decker, R. B., Krimigis, S. M., Roelof, E. C., et al. 2008, Natur, 454, 67
Decker, R. B., Krimigis, S. M., Roelof, E. C., & Hill, M. E. 2012, Natur, 489, 124
Donoho, D. L. 2006, ITIT, 52, 1289
Drake, J. F., Opher, M., Swisdak, M., & Chamoun, J. N. 2010, ApJ, 709, 963
Drake, J. F., Swisdak, M., Opher, M., & Richardson, J. D. 2017, ApJ, 837, 159
Fisk, L. A., & Gloeckler, G. 2008, ApJ, 686, 1466
Fraternale, F. 2017, PhD thesis, Politecnico di Torino
Fraternale, F., Gallana, L., Iovieno, M., et al. 2016, PhyS, 91, 394
Frisch, U. 1995, Turbulence: The Legacy of AN Kolmogorov (Cambridge: Cambridge Univ. Press)
Gallana, L., Fraternale, F., Iovieno, M., et al. 2016, JGRA, 121, 3905
Goldreich, P., & Sridhar, S. 1995, ApJ, 438, 763
Goldreich, P., & Sridhar, S. 1997, ApJ, 485, 680
Goldstein, M. L., Smith, C. W., & Matthaeus, W. H. 1983, JGR, 88, 9989

Gurnett, D. A., Kurth, W. S., Burlaga, L. F., & Ness, N. F. 2013, Sci, 341, 1489
Gurnett, D. A., Kurth, W. S., Stone, E. C., et al. 2015, ApJ, 809, 121
Hadid, L. Z., Sahraoui, F., Galtier, S., & Huang, S. Y. 2018, PhRvL, 120, 055102
Heerikhuisen, J., & Pogorelov, N. V. 2011, ApJ, 738, 29
Heerikhuisen, J., Pogorelov, N. V., Zank, G. P., et al. 2010, ApJL, 708, L126
Heerikhuisen, J., Zirnstein, E. J., Funsten, H. O., Pogorelov, N. V., & Zank, G. P. 2014, ApJ, 784, 73
Hill, M. E., Decker, R. B., Brown, L. E., et al. 2014, ApJ, 781, 94
Howes, G. G., Klein, K. G., & TenBarge, J. M. 2014, ApJ, 789, 106
Iovieno, M., Gallana, L., Fraternale, F., et al. 2016, EJMF, 55, 394
Izmodenov, V., Alexashov, D., & Myasnikov, A. 2005, A&A, 437, L35
Izmodenov, V. V., & Alexashov, D. B. 2015, ApJS, 220, 32
Izmodenov, V. V., Malama, Y. G., Ruderman, M. S., et al. 2009, SSRv, 146, 329
Katushkina, O. A., Izmodenov, V. V., & Alexashov, D. B. 2015, MNRAS, 446, 2929
Kim, T. K., Pogorelov, N. V., & Burlaga, L. F. 2017, ApJL, 843, L32
Kolmogorov, A. N. 1941, DoSSR, 30, 301
Krimigis, S. M., Roelof, E. C., Decker, R. B., & Hill, M. E. 2011, Natur, 474, 359
Macek, W. M., & Wawrzaszek, A. 2013, NPGeo, 20, 1061
Macek, W. M., Wawrzaszek, A., & Burlaga, L. F. 2014, ApJL, 793, L30
Macek, W. M., Wawrzaszek, A., & Carbone, V. 2012, JGRA, 117, A12101
Matthaeus, W. H., & Goldstein, M. L. 1982, JGR, 87, 6011
Matthaeus, W. H., & Goldstein, M. L. 1986, PhRvL, 57, 495
Matthaeus, W. H., Goldstein, M. L., & Roberts, D. A. 1990, JGRA, 95, 20673
Meneveau, C., & Sreenivasan, K. R. 1987, NuPhS, 2, 49
Monin, A. S., & Yaglom, A. M. 1971, Statistical Fluid Mechanics, Vol. 2 (Cambridge, MA: MIT Press)
Montroll, E. W., & Shleisinger, M. F. 1982, PNAS, 79, 3380
Muller, W. C., & Biskamp, D. 2000, PhRvL, 84, 475
Opher, M. 2016, SSRv, 200, 475
Opher, M., Drake, J. F., Schoeffler, K. M., et al. 2011, ApJ, 734, 71
Perez, J., & Chandran, B. D. G. 2013, ApJ, 776, 124
Pogorelov, N. V., Bedford, M. C., Kryukov, I. A., & Zank, G. P. 2016, JPhCS, 767, 012020
Pogorelov, N. V., Borovikov, S. N., Heerikhuisen, J., & Zhang, M. 2015, ApJL, 812, L6
Pogorelov, N. V., Borovikov, S. N., Zank, G. P., et al. 2012, ApJL, 750, L4
Pogorelov, N. V., Borovikov, S. N., Zank, G. P., & Ogino, T. 2009a, ApJ, 696, 1478
Pogorelov, N. V., Fichtner, H., Czechowski, A., et al. 2017a, SSRv, 212, 193
Pogorelov, N. V., Heerikhuisen, J., Mitchell, J. J., Cairns, I. H., & Zank, G. P. 2009b, ApJL, 695, L31
Pogorelov, N. V., Heerikhuisen, J., Roytershteyn, V., et al. 2017b, ApJ, 845, 9
Pogorelov, N. V., Heerikhuisen, J., & Zank, G. P. 2008, ApJL, 675, L41
Pogorelov, N. V., Suess, S. T., Borovikov, S. N., et al. 2013, ApJ, 772, 2
Politano, H., & Pouquet, A. 1995, PhRvE, 52, 636
Politano, H., & Pouquet, A. 1998, PhRvE, 57, R21
Politano, H., Pouquet, A., & Carbone, V. 1998, EL, 43, 516
Richardson, J. D. & the Voyager Team 2016, in AIP Conf. Proc. 1720, SOLAR WIND 14: Proceedings of the Fourteenth International Solar Wind Conference, ed. L. Wang et al. (Melville, NY: AIP), 080001
Richardson, J. D., & Burlaga, L. F. 2013, SSRv, 176, 217
Richardson, J. D., Burlaga, L. F., Drake, J. F., Hill, M. E., & Opher, M. 2016, ApJ, 831, 115
Richardson, J. D., & Decker, R. B. 2014, ApJ, 792, 126
Richardson, J. D., & Decker, R. B. 2015, J. Phys. Conf. Ser., 577, 012021
Roberts, D. A. 2010, JGRA, 115, A12101
Roberts, D. A., Klein, L. W., Goldstein, M. L., & Matthaeus, W. H. 1987, JGR, 92, 11021
Schekochihin, A. A., Cowley, S. C., Dorland, W., et al. 2009, ApJS, 182, 310
Schwadron, N. A., Adams, F. C., Christian, E. R., et al. 2014, Sci, 343, 988
Schwadron, N. A., & McComas, D. J. 2013, ApJL, 778, L33
She, Z.-S., & Leveque, E. 1994, PhRvL, 72, 336
Smith, C. W., Goldstein, M. L., & Matthaeus, W. H. 1983, JGR, 88, 5581
Smith, C. W., Hamilton, K., Vasquez, B. J., & Leamon, R. J. 2006a, ApJL, 645, L85
Smith, C. W., Isenberg, P. A., Matthaeus, W. H., & Richardson., J. D. 2006b, ApJ, 638, 508
Sorriso-Valvo, L., Carbone, F., Leonardis, E., et al. 2017, AdSpR, 59, 1642
Sorriso-Valvo, L., Carbone, F., Perri, S., et al. 2018, SoPh, 293, 10
Sorriso-Valvo, L., Catapano, F., Retinò, A., et al. 2019, PhRvL, 122, 035102
Sorriso-Valvo, L., Marino, R., Carbone, V., et al. 2007, PhRvL, 99, 115001
Stone, E. C., Cummings, A. C., McDonald, F. B., et al. 2005, Sci, 309, 2017
Stone, E. C., Cummings, A. C., McDonald, F. B., et al. 2008, Natur, 454, 71
Stone, E. C., Cummings, A. C., McDonald, F. B., et al. 2013, Sci, 341, 150
Taylor, G. I. 1938, RSPSA, 164, 476
Tenerani, A., & Velli, M. 2017, ApJ, 843, 26
Tu, C.-Y., Pu, Z.-Y., & Wei, F.-S. 1984, JGR, 89, 9695
Velli, M., Grappin, R., & Mangeney, A. 1989, PhRvL, 63, 1807
Webber, W. R., & McDonald, F. B. 2013, GeoRL, 40, 1665
Zank, G. P. 1999, SSRv, 89, 413
Zank, G. P. 2015, ARA&A, 53, 449
Zank, G. P., Du, S., & Hunana, P. 2017, ApJ, 842, 114
Zank, G. P., Heerikhuisen, J., Pogorelov, N. V., Burrows, R., & McComas, D. 2010, ApJ, 708, 1092
Zhang, M., & Pogorelov, N. V. 2016, J. Phys. Conf. Ser., 767, 012027
Zhang, M., Zuo, P., & Pogorelov, N. V. 2014, ApJ, 790, 5
Zirnstein, E. J., Heerikhuisen, J., Funsten, H. O., et al. 2016, ApJL, 818, L18
Zirnstein, E. J., Heerikhuisen, J., & McComas, D. J. 2015a, ApJL, 804, L22
Zirnstein, E. J., Heerikhuisen, J., McComas, D. J., et al. 2018, ApJ, 859, 104
Zirnstein, E. J., Heerikhuisen, J., Pogorelov, N. V., McComas, D. J., & Dayeh, M. A. 2015b, ApJ, 804, 5
Zirnstein, E. J., Heerikhuisen, J., Zank, G. P., et al. 2017, ApJ, 836, 238